Global Emissions Inventory from Open Biomass Burning (GEIOBB): Utilizing Fengyun–3D global fire spot monitoring data

Yang Liu[1,2], Jie Chen[3,4], Yusheng Shi[1], Wei Zheng[3,4], Tianchan Shan[3,4], Gang Wang[5]

[1]State Key Laboratory of Remote Sensing Science, Aerospace Information Research Institute, Chinese Academy of Sciences, Beijing, 100101, China
[2]College of Resources and Environment, University of Chinese Academy of Sciences, Beijing, 101408, China
[3]Innovation Center for FengYun Meteorological Satellite, National Satellite Meteorological Center (National Center for Space Weather), China Meteorological Administration, Beijing 100081, China
[4]Key Laboratory of Radiometric Calibration and Validation for Environmental Satellites, National Satellite Meteorological Center (National Center for Space Weather), China Meteorological Administration, Beijing 100081, China
[5]Guangzhou Meteorological Satellite Ground Station, National Satellite Meteorological Center (National Center for Space Weather), China Meteorological Administration, Guangzhou 510640, China

Correspondence to: Yusheng Shi (shiys@aircas.ac.cn), Tianchan Shan (shantc9165@163.com)

Abstract: Open biomass burning (OBB) significantly affects regional and global air quality, climate change, and human health. It is susceptible to fire types, including forests, shrublands, grasslands, peatlands, and croplands burning. Global high–resolution satellites can detect active fires, enabling a more accurate estimation of these emissions. In this study, we developed a global high–resolution (1×1 km) daily emission inventory associated with OBB emissions using the Chinese Fengyun–3D satellite's global fire spot monitoring data, satellite and observational biomass data, vegetation index–derived spatiotemporal variable combustion efficiencies, and land–type–based emission factors. The average annual OBB emissions for 2020–2022 were 2,586.88 Tg C, 8841.45 Tg CO_2, 382.96 Tg CO, 15.83 Tg CH_4, 18.42 Tg NO_X, 4.07 Tg SO_2, 18.68 Tg OC, 3.77 Tg BC, 5.24 Tg NH_3, 15.85 Tg NO_2, 42.46 Tg $PM_{2.5}$ and 56.03 Tg PM_{10}. Specifically, taking carbon emissions as an example, the average annual OBB for 2020–2022 were 72.71 (Boreal North America; BONA), 165.7 (Temperate North America, TENA), 34.1 (Central America; CEAM), 42.9 (Northern Hemisphere South America; NHSA), 520.5 (Southern Hemisphere South America; SHSA), 13 (Europe; EURO), 8.4 (Middle East; MIDE), 394.3 (Northern Hemisphere Africa; NHAF), 847 (Southern Hemisphere Africa; SHAF), 167.4 (Boreal Asia; BOAS), 27.9 (Central Asia; CEAS), 197.3 (Southeast Asia; SEAS), 13.2 (Equatorial Asia; EQAS), and 82.4 (Australia and New Zealand; AUST) Tg. SHAF was identified as the region with the largest emissions. Notably, savanna grassland accounted for the lion's share of total emissions, contributing to 46%, followed by woody savanna/shrubs at 33%. Moreover, notable seasonal variability characterizes the OBB carbon emissions, with marked increases observed in August and September (annual average 441.32 Tg C) compared to other months (annual average 170.42 Tg C). This surge in carbon emissions is chiefly attributed to fires in the savanna grasslands, woody savanna/shrubs, and tropical forests of SHAF, SHSA, and NHAF. Fires in savanna grasslands were predominant in the NHAF, contributing to 77% of emissions during January–April, whereas in the SEAS, woody savanna/shrubs (52%) and tropical forests (23%) were the

primary sources. Our comprehensive high–resolution inventory of OBB emissions provides valuable insights for enhancing the accuracy of air quality modelling, atmospheric transport and biogeochemical cycle studies.

1 Introduction

Open biomass burning (OBB) releases significant amounts of trace gases (CO, NO_X, NMVOC, SO_2, and NH_3), particulate matter ($PM_{2.5}$, PM_{10}), and greenhouse gases (CH_4 and CO_2), which are major sources of atmospheric pollutants (Mehmood et al., 2022) and have profound impacts on the global carbon cycle, climate change, and air quality, thus exerting a significant influence on the global environment and human health (Wu et al., 2022). Forest clearing, accidental fires, firewood burning, agricultural residue burning, peatland burning and straw burning are among the major fire types worldwide (van der Werf et al., 2017). These open burning activities severely impact air quality and ecosystems (Anon, 2017), with a high degree of sporadicity and spatiotemporal clustering (Liu et al., 2014; Murdiyarso and Lebel, 2007; Senande-Rivera et al., 2022). However, some regions worldwide are experiencing a notable increase in fire incidents (Richardson et al., 2022), such as, the Amazon rainforest fires (Pivello, 2011), Australian bushfires (Jegasothy et al., 2023), and wildfires in the United States (You and Xu, 2023), which are large–scale fire incidents that occur multiple times annually. Therefore, accurately estimating these emissions is crucial for devising effective environmental policies and better safeguarding people's health and quality of life, providing significant support for a sustainable future.

Previous studies have investigated numerous methods for estimating biomass burning emissions (Ito and Penner, 2004; Wiedinmyer et al., 2006). The burned area method demonstrated good accuracy in quantifying larger fire events, which is based on the burned area, the available biomass fuels burned in fields, the fuel-related combustion efficiency, and emission factors. For instance, Shi et al. (2020) estimated OBB emissions in tropical continents from 2001 to 2017. As well as other open-access databases, such as the Global Fire Emissions Database (GFED) and the Fire INventory from NCAR (FINN) (Jiang et al., 2012; van Wees et al., 2022). However, this method relies heavily on fire detection precision, particularly for small fires. Alternatively, a method based on the fire radiative power can effectively enhance the assessment of small fire events, thereby addressing this issue to a certain extent. For example, similar approaches have been employed in Fire Emissions and Energy Research (FEER) and the Global Fire Assimilation System (GFAS) (Di Giuseppe et al., 2017). However, this approach has a drawback in that it tends to overestimate emissions during localized fire events. Nonetheless, all these methods rely on MODIS active fire products.

Equipped with the MERSI–2 instrument, the Fengyun–3D (FY–3D) satellite offers spatial resolutions of 250 and 1000 m at the nadir (Zhenzhen Yin, 2020), which, when compared to MODIS, significantly enhances its capacity to detect and analyze various phenomena, including fires, aerosols, and changes in land and ocean surfaces (Zheng et al., 2023). Furthermore, the Global Fire Monitoring (GFR) product with FY–3D employs optimized automatic identification algorithms for fire spots (Shan and Zheng, 2022), leading to an improved accuracy of fire point detection. This resulted in an impressive overall accuracy rate of 79.43% and an exclusion omission error accuracy of 88.50%, surpassing the capabilities of MODIS satellite products (Chen et al., 2022; Xian et al., 2021), based on field–collected references throughout 2020 in China. The cross–verification between MODIS and FY–3D shows the highest consistency results (over 80%) in Africa and Asia, while America, Europe, and Oceania demonstrate consistency exceeding 70% (Chen et al., 2022). In July, August, and September, the number of fire spots was higher, with a mean consistency of over 85% between MODIS and FY–3D fire products (Chen et al., 2022). Although Landsat Fire and Thermal Anomaly (LFTA) product has finer spatial resolution, its lower temporal resolution typically allows global coverage only every 16 days, which does not allow for frequent detection of biomass burning activity. Therefore, employing the FY–3D GFR product and allocation approaches for small fires is expected to yield reliable estimates of OBB emissions.

Fuel loading (F) represents the ground biomass of fire–affected pixels. Many studies treat F as a constant based on regional land cover types, neglecting the actual spatial and temporal variability (Wiedinmyer et al., 2011). Similarly, the combustion factor (CF), which represents the proportion of small biomass burned in a fire event, is typically assumed to be constant without considering the fuel status and humidity conditions (Pfeiffer et al., 2013). However, this approach leads to increased uncertainty in biomass estimation and poor quantification of the extent of combustion during fire events, thereby affecting the assessment of OBB emissions (Shi et al., 2020). To address these issues, this study employed observational and satellite–based aboveground biomass (AGB) and CF based on time series data of the vegetation index derived from satellite products. This CF considers moisture–related factors, enabling the calculation of the spatiotemporal variance in combustion efficiency across diverse land types.

This study aimed to develop a high–resolution daily OBB emissions inventory (including carbon (C), carbon dioxide (CO_2), carbon monoxide (CO), methane (CH_4), nitrogen oxides (NO_X), sulfur dioxide (SO_2), particulate organic carbon (OC), particulate black carbon (BC), ammonia (NH_3), nitrogen dioxide (NO_2), $PM_{2.5}$, PM_{10}) and analyze the various types of fire events along with their emission patterns across 14 distinct regions. To estimate OBB emissions form forests, savannas/shrublands, grasslands, and peatlands, we utilized the updated FY–3D GFR product based on the continuous spatiotemporal dynamics of AGB, spatially and temporally variable combustion efficiencies, and emission factors specific to different land types. Our comprehensive high–resolution inventory of OBB emissions represents a valuable asset for applications in air quality modelling, atmospheric transport simulations, and biogeochemical cycling studies. This provides a robust framework for an in–depth understanding and analysis of the environmental implications of OBB on a global scale.

2 Materials and Methods

The global Emissions Inventory from Open Biomass Burning (GEIOBB) (1 km daily) was estimated using the burned area method based on the framework described by Widinmyer et al. (2006) and Shi et al. (2015). GEIOBB conducts of OBB emissions using burned areas retrieved from active fire data from the FY–3D satellite, available biomass from satellite and ground measurements, CF scaled by tree cover and NDVI (Normalized Difference Vegetation Index), and land cover–based emission factors. The GEIOBB is obtained by calculating the product of the above terms.

$$E_i(x) = B(x,t) \times F(x) \times CF(x) \times EF(i), \tag{1}$$

where E_i (g/m^2) represents type i emissions at location x, which is equal to the product of the burning area B (m^2) at time t and location x, biomass F ($g\ C/m^2$) at location x, CF (expressed as a *fraction*), and the emission factor EF (g/kg) for type i pollutants.

2.1 FY–3D global fire spot monitoring data based burned area (B)

The Fengyun–3 series of satellites is a second–generation Chines polar–orbiting meteorological satellites. The FY–3D satellite is the fourth satellite of the FY–3 series of satellites. It is at an altitude of 836 km and was launched on November 15, 2017 and published on may, 2020. (Li et al., 2017). FY–3D completes 14 orbital observations of the Earth's surface at a global scale twice daily. The MERSI–2 instrument onboard with FY–3D was greatly improved from MERSI–1 with FY–3C, with high accuracy of onboard and lunar calibration capabilities. Compared to MODIS, FY–3D fire products have been optimized in terms of auxiliary parameters, fire identification and re–identification. Firstly, FY–3D introduces the adaptive threshold and eliminates the limitations by fixed thresholds of MODIS and VIIRS algorithms by automatic identification algorithms for fire spot detection (Chen et al., 2022). Secondly, FY–3D uses a re–identification index reflecting varying geographical latitude and underlying surfaces types, together with the effect by cloud, water, and bare land (Zheng et al., 2020). The integration of multiple influencing factors increases the accuracy of fire detection. For example, the influences of factory thermal anomalies and high reflectance of photovoltaic power plants are greatly removed. Finally, the far–infrared channel employed in FY–3D has a high resolution of 250 m, higher than MODIS with 1 km, resulting in higher accuracy in big fire detection (Zheng and Chen, 2020). Overall, the FY–3D GFR product achieves an accuracy of 94.0% globally, with accuracies of 94.6%, 94.1%, 90.6%, 91.8%, and 92.7% in South–central Africa, East central South America, Siberia, Australia and Indochinese Peninsula (Chen et al., 2022), respectively. Specifically, due to the removal of underlying surface interference in China, the FY-3D achieves accuracies of 79.43% and 88.50% for accuracy and accuracy without omission, respectively, both of which are higher than the accuracies of 74.23% and 79.69% achieved by MODIS (Chen et al., 2022).

Here, the location and timing of the fire events used in the GEIOBB were determined globally using the FY–3D GFR product (Chen et al., 2022). These processed fire event detection data were available from the Fengyun Satellite Remote Sensing Data Service Network of National Satellite Meteorological Centre (http://satellite.nsmc.org.cn/PortalSite/Default.aspx). These data offer daily fire detection at 1–km resolution, including the location, time, and confidence level of fire detection at a confidence level greater than 20% (Liu and Shi, 2023). Furthermore, multiple counts of the same fire may be made on a single day, leading to duplication of the data. To address this issue, we performed global identification and removed multiple detections of the same fire pixels daily. Specifically, we removed single daily fire detections within a 1 km^2 radius of another fire detection. Thus, only one fire per 1 km^2 of a hotspot can be counted per day and reset the next day.

Table 1. Comparison of parameters related to MERSI–2, MODIS, and VIIRS.

	MERSI–2 (FY–3D)	MODIS (AQUA)	VIIRS ((NOAA–20))
Orbit altitude (km)	836	705	824

Equator Crossing time	14:00 LT	13:30 LT	14:20 LT
Swath (km)	2900	2330	3060
Pixel resolution at nadir (km)	1	1	0.75/0.375
Pixel resolution at the edge (km)	>6	4	1.5/0.75
ID MIR Band (s)	21	21/22	M–13/I–4
Spectral range (μm)	3.973–4.128	3.929–3.989 3.940–4.001	3.973–4.128 3.550–3.930
TMAX (SNR–NEΔT on orbit)	380 K (0.25)	500 K (0.183) 331 K (0.019)	634 K (0.04)
ID TIR Band (s)	24	31	M–15/I–5
Spectral range (μm)	10.300–11.300	10.780–11.280	10.263–11.263 10.500–12.400
TMAX (SNR–NEΔT on orbit)	330 K (0.4)	400 K (0.017)	343 K (0.03)

2.2 Fuel loading (F)

Previous studies on emission inventories based on wildfire areas were mostly used to assess F by defining different fire types in different areas (Wiedinmyer et al., 2011). The data generated by this method have some discontinuities, which may lead to large deviations at the boundaries of different areas, which is unreasonable and does not reflect the spatial distribution pattern of F. Ground observation data have advantages in terms of accuracy and reliability but are limited by the sparse distribution of observation stations, preventing comprehensive global coverage. In contrast, satellite data cover the entire globe and provide surface parameters worldwide, thereby enabling biomass estimation. However, its accuracy and usability are limited by factors, such as temporal and spatial resolution and cloud cover. Therefore, fusion of ground observations with satellite data is an effective solution. This fusion method combines the high accuracy of ground observation data with wide coverage of satellite data to produce reliable and precise global biomass products. Using this method, it is possible to overcome the limitations of a single data source, thereby enhancing the accuracy and reliability of biomass estimation.

This study used multi–source data, including NDVI, tree cover (TC), and satellite and observational AGB, to assess terrestrial biomass, in which TC data were derived from the MOD44B product (DiMiceli et al., 2022) generated based on MODIS onboard the Terra satellite (https://lpdaac.usgs.gov/products/mod44bv061/), which provides a continuous global vegetation field at 250m resolution for each year from 2000 to the present. The NDVI data were obtained using the MODIS Combined 16–Day NDVI fusion product available on the GEE platform. AGB shows a large linear correlation with TC and NDVI (Xingcheng et al., 2017), so we combined the global aboveground and belowground biomass carbon density maps for the 2010 product (https://daac.ornl.gov/cgi-bin/dsviewer.pl?ds_id=1763) provided by Spawn and Gibbs(2020), annual TC, and NDVI data, and obtained by linear stretching the fuel loading for other years.

$$F(x,t) = \left(\frac{NDVI_{now}}{NDVI_{2010}} + \frac{TC_{now}}{TC_{2010}}\right) * AGB \tag{2}$$

Where $NDVI_{now}$ is the mean value of the month before a single fire event, $NDVI_{2010}$ is the mean value of *NDVI* in 2020, TC_{now} is the tree cover in the year of the fire incident, TC_{2010} is the tree cover in 2020, and *AGB* is the Above Ground Biomass data in 2010.

2.3 Combustion factor (CF)

The CF is mainly defined as the percentage of fuel consumed during individual fire events, which primarily depends on the type of fuel and humidity conditions. Typically, CF is set as a constant, which may lead to biases in emission estimations and generate significant uncertainties. Although some studies have utilized TC to quantify CF and explain its spatial and temporal variations (Wiedinmyer et al., 2006; Qiu et al., 2016; Bray et al., 2018; Wu et al., 2018), prior research has mainly focused on areas with herbaceous vegetation cover, where TC ranges from 40% to 60%. They assumed that the CF remained consistent across other land types, such as farmlands, forests, and grasslands.

A major influence on fire discharge in the framework is the surface condition at the location of the fire event. Different land types exhibit different biological qualities and correlations. In GEIOBB, we used International Geosphere–Biosphere Programme (IGBP) categorized data from MODIS land cover type (LCT) (Friedl and Sulla-Menashe, 2022) (MCD12Q1, https://lpdaac.usgs.gov/products/mcd12q1v061/), reclassified the original 17 classifications, and reclassified the results to reorganize the subsurface types into seven categories, including grasslands and savannas (V1), woody savannas or shrubs (V2), tropical forests (V3), temperate forests (V4), boreal forests (V5), temperate evergreen forests (V6), and crops (V7), to allow for better matching in subsequent assignments of biomass and related factors. In the GEIOBB, the CF of all fires in each grid cell were allocated as a function of TC, fire types, and NDVI (Ito and Penner, 2004). The CF calculations are segmented into four categories based on the reclassification results. Specifically, we amalgamated the reclassification outcomes of V3, V4, V5, and V6 into a forest type category, designated V1 and V2 as woodlands, and assigned V7 to crops (the specific classification method is elaborated in detail in Supplementary Information (SI) Table S1 and Section S1).

For woodlands, the CF was highly correlated with *TC*(Ito and Penner, 2004):

$$CF_{woodland} = EXP(-0.013 \times TC). \tag{3}$$

For grasslands, we introduced the vegetation condition index (*VCI*) to determine the fuel moisture conditions, which were used to measure vegetation drought conditions. We incorporated the *VCI* to ascertain fuel moisture conditions, which served as a metric for assessing the contemporaneous conditions of vegetation. The *VCI* was computed using the *NDVI* with a time interval of 16 d at a spatial resolution of 1 km for the period 2020–2022(Ito and Penner, 2004).

$$vci = \frac{NDVI_{now} - NDVI_{min}}{NDVI_{max} - NDVI_{min}}, \tag{4}$$

$$CF_{grassland} = TC \times (-2.13 \times VCI + 1.38) + (0.9 - TC). \quad (5)$$

where $NDVI_{now}$ is the mean value of the month before a single fire event, $NDVI_{max}$ the maximum value of $NDVI$ in the same period in the previous 3 years, and $NDVI_{min}$ is the minimum value of $NDVI$ in the same period in the previous 3 years.

For forests, we used moisture category factors (*MCF*) to measure forest moisture, conducted an analysis based on the partitioning provided (Ito and Penner, 2004), and discovered that it approximately conforms to the power function distribution characteristics in *VCI*. Subsequently, function fitting was executed ($R^2 = 0.94$), through which we further determined *CF*. For grasslands, the *VCI* could be directly calculated and utilized.

$$MCF = 0.1759 \times e^{3.5181 \times VCI}, \quad (6)$$

$$CF_{forest} = (1 - e^{-1})^{MCF}. \quad (7)$$

Most fires on croplands are artificially active fires, which result in a full combustion process that is not designed for woody fuels. Therefore, we set the *CF* for crops to 0.98, the upper limit proposed by Wiedinmyer (2006).

2.4 Emission factor (EF)

EF denotes the amount of pollutants released per unit of fuel burned during burning. Here, EF in Tabel 2 was assigned according to the LCT (Akagi et al., 2011; van Leeuwen et al., 2014; Liu et al., 2017; Paton-Walsh et al., 2014; Urbanski, 2014; Fang et al., 2017). However, other EF measurements were also used when locally measured EF data were not available. The land types in all fire pixels were determined by reclassification of the LCT product. We used the IGBP LCT classification to assign each fire pixel to one of the land–use/land–cover classes. Here, owing to significant variations among the measured values, we took the average emission factor within each reclassification type for areas with multiple measurements. Finally, the EF for the following seven land types of other database were updated: grasslands and savannas, woody savanna or shrubs, tropical forest, temperate forest, boreal forest, temperate evergreen forest, and crop.

Table 2. Emission factor (g/kg) of different species.

Species	Grasslands and Savannas	Woody Savanna or Shrubs	Tropical Forest	Temperate Forest	Boreal Forest	Temperate Evergreen Forest	Crop			
							Maize	Sugar	Sugar	Wheat
C	488.31	489.41	491.77	468.31	478.88	493.18	687.09	323.35	368.04	429.17
CO_2	1,686[a]	1,681[a]	1,643[a]	1,510[a]	1,565[b]	1,623[a]	2,327[c]	1,130[c]	1,177[c]	1,470[e]
CO	63.00[a]	67.00[a]	93.00[a]	122.00[a]	111.00[b]	112.00[a]	114.70[c]	34.70[c]	93.00[c]	60.00[e]
CH_4	2.00[a]	3.00[a]	5.10[a]	5.61[a]	6.00[b]	3.40[a]	4.40[c]	0.40[c]	9.59[c]	3.40[e]
NO_X	3.90[a]	3.65[a]	2.60[a]	1.04[a]	0.95[b]	1.96[a]	4.30[c]	2.60[c]	2.28[c]	3.30[e]
SO_2	0.90[a]	0.68[a]	0.40[a]	1.10[a]	1.00[b]	1.10[a]	0.44[c]	0.22[c]	0.18[c]	0.85[e]
OC	2.60[a]	3.70[a]	4.70[a]	7.60[a]	7.80[b]	7.60[a]	2.25[c]	3.30[c]	2.99[c]	3.90[d]
BC	0.37[a]	1.31[a]	0.52[a]	0.56[a]	0.20[b]	0.56[a]	0.78[d]	0.82[d]	0.52[d]	0.52[d]
NH_3	0.56[a]	1.20[a]	1.30[a]	2.47[a]	1.80[b]	1.17[a]	0.68[c]	1.00[c]	4.10[c]	0.37[e]
NO_2	3.22[a]	2.58[a]	3.60[a]	2.34[a]	0.63[b]	2.34[a]	2.99[f]			

$PM_{2.5}$	7.17[a]	7.10[a]	9.90[a]	15.00[a]	18.40[b]	17.90[a]		6.43[f]
PM_{10}	7.20[a]	11.4[a]	18.50[a]	16.97[a]	18.40[b]	18.40[a]		7.02[f]

All the value of C were Calculated by CO_2, CO, and CH_4.

[a] is average value from (Akagi et al., 2011).

[b] is average from (Akagi et al., 2011) and (Urbanski, 2014).

[c] is average from (Akagi et al., 2011; Fang et al., 2017; Liu et al., 2016; Santiago-De La Rosa et al., 2018; Stockwell et al., 2015).

[d] is from (Kanabkaew and Kim Oanh, 2011).

[e] is from (Cao et al., 2008).

[f] is from (Li et al., 2007).

3 Results and Discussions

3.1 Spatial map of OBB emission estimates

We estimated global OBB emissions using GEIOBB, and the average annual OBB emissions for 2020–2022 were 2586.88 Tg C, 3.77 Tg BC, 15.83 Tg CH_4, 382.96 Tg CO, 8841.45 Tg CO_2, 5.24 Tg NH_3, 15.85 Tg NO_2, 18.42 Tg NO_X, 18.68 Tg OC, 56.03 Tg PM10, 42.46 Tg PM2.5, and 4.07 Tg SO_2 (Table 3). Taking carbon as an example, the annual carbon emissions from OBB were estimated for the period of 2020–2022 (Figure 1) and the total OBB carbon emissions reached 7760.63 Tg C. The average annual carbon emissions during this period amounted to 2586.88 Tg. Overall, obvious spatial variations in the OBB carbon emissions were observed across Africa, and certain regions in the Americas and Asia. In America, elevated emissions were observed in central and northeastern Brazil, northern Bolivia, northern Paraguay, eastern Mexico, and much of Honduras. In Africa, substantial OBB emissions originated from Central Africa (excluding the Democratic Republic of the Congo), the northern regions of West Africa, and the southern regions of East Africa, where most 1 km×1 km grid cells exhibited annual average carbon emissions exceeding 50 g C/m². Elevated carbon emissions were found in Southeast Asia (the Indo–Chinese Peninsula), with significant emissions detected in western and eastern Myanmar, northern Laos, eastern Cambodia, southern Nepal, and parts of northern India. Notable carbon emissions were also observed in equatorial Asia, South Sumatra, South Kalimantan, and southern Papua New Guinea.

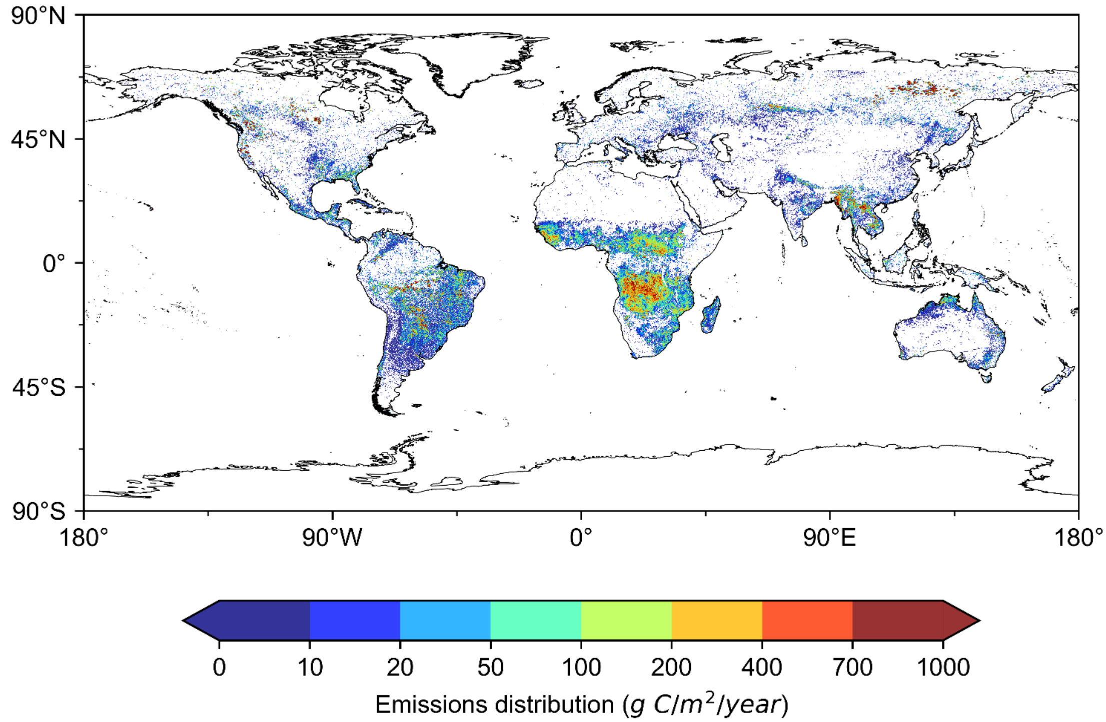

Figure 1: Spatial distribution of annual average of OBB carbon emissions (1 km×1 km) during 2020–2022.

Table 3. Global OBB annual emissions and region–specific average annual emissions during 2020–2022 (Tg–Species/year).

	C	BC	CH_4	CO	CO_2	NH_3	NO_2	NO_X	OC	PM_{10}	$PM_{2.5}$	SO_2
2020	2,861.05	4.09	17.39	423.12	9,777.79	5.76	17.58	20.37	20.64	61.59	47.18	4.54
2021	2,991.16	4.52	18.22	439.67	10,226.55	6.11	18.17	21.36	21.64	64.76	48.89	4.70
2022	1,908.42	2.69	11.87	283.09	6,520.04	3.87	11.82	13.53	13.74	41.76	31.31	2.97
average	2,586.88	3.77	15.83	381.96	8,841.46	5.24	15.85	18.42	18.68	56.03	42.46	4.07
BONA	72.71	0.16	0.49	10.92	248.08	0.18	0.36	0.49	0.63	1.80	1.29	0.11
TENA	165.73	0.30	1.02	26.14	563.78	0.38	0.92	1.11	1.45	3.98	3.18	0.28
CEAM	34.11	0.06	0.23	5.21	116.26	0.08	0.20	0.23	0.27	0.81	0.56	0.05
NHSA	42.93	0.06	0.28	6.42	146.58	0.08	0.28	0.30	0.31	1.01	0.70	0.06
SHSA	520.55	0.61	3.74	83.09	1,767.83	1.12	3.42	3.45	4.01	13.00	9.08	0.74
EURO	13.02	0.02	0.09	2.02	44.33	0.03	0.08	0.09	0.09	0.26	0.22	0.02
MIDE	8.37	0.01	0.06	1.28	28.54	0.02	0.05	0.06	0.05	0.15	0.13	0.01
NHAF	394.25	0.41	2.05	54.58	1,354.19	0.62	2.56	2.99	2.39	7.01	6.01	0.66
SHAF	847.03	1.28	4.52	116.23	2,910.72	1.52	5.17	6.40	5.55	16.48	12.82	1.38
BOAS	167.35	0.31	0.98	23.57	573.90	0.35	0.93	1.22	1.22	3.53	2.68	0.27
CEAS	27.93	0.04	0.21	4.55	94.68	0.08	0.17	0.19	0.20	0.56	0.47	0.04
SEAS	197.29	0.37	1.54	32.49	668.10	0.55	1.16	1.26	1.71	5.24	3.50	0.28
EQAS	13.20	0.03	0.10	2.04	44.94	0.03	0.08	0.09	0.11	0.36	0.22	0.02

AUST	82.38	0.11	0.52	13.41	279.54	0.19	0.48	0.54	0.70	1.83	1.59	0.15

Additionally, we divided the world into 14 regions for analysis and discussion, the geographical regions is same as (van der Werf et al., 2017). As delineated by the reclassification in Figure 2(b), savanna grasslands have emerged as the predominant LCT worldwide, encompassing 53.30% of total coverage. This type primarily spans South America, most of Africa, and Asia. Following closely is woody savanna account for 19.74% of the global coverage. They are predominantly situated in Boreal Asia, Australia, selected areas of southern Africa, and parts of North America. The third most prevalent type was tropical forest, comprising 9.03%, with its main distribution in South America, notably within the Amazon Rainforest, regions adjacent to the African equator, and Southeast Asia. Other types, such as temperate forest, boreal forest, temperate evergreen forest, and crops, are less extensively spread and exhibit a more dispersed distribution.

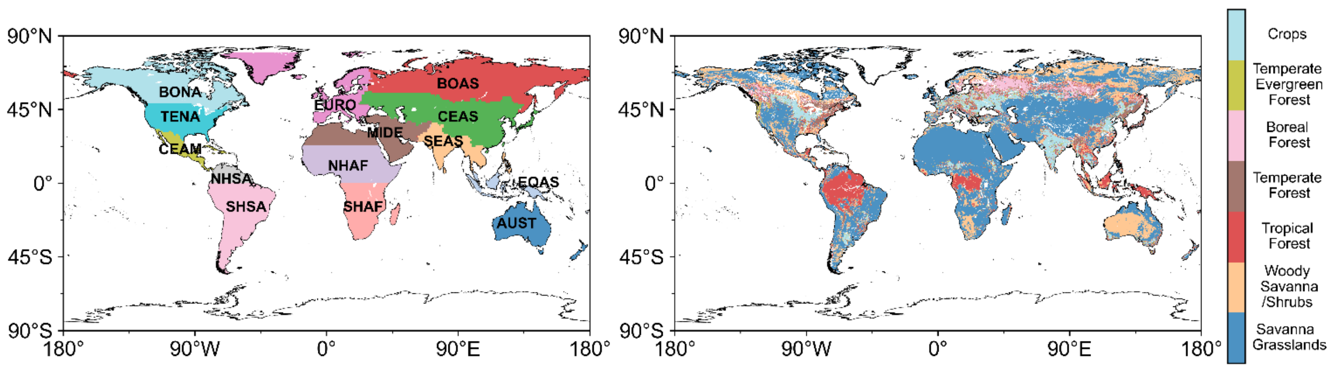

Figure 2 (a) Global geographic regions and its abbreviations. The acronyms on the figure represent the following: BONA: Boreal North America; TENA: Temperate North America; CEAM: Central America; NHSA: Northern Hemisphere South America; SHSA: Southern Hemisphere South America; EURO: Europe; MIDE: Middle East; NHAF: Northern Hemisphere Africa; SHAF: Southern Hemisphere Africa; BOAS: Boreal Asia; CEAS: Central Asia; SEAS: Southeast Asia; EQAS: Equatorial Asia; AUST: Australia and New Zealand;(b) Global land cover type reclassification.

Then, this study quantified the global average annual OBB carbon emissions from different regions and fire types during 2020–2022 (Table 4). Southern Hemisphere Africa (SHAF) was found to be the primary source of global OBB carbon emissions (847.04 Tg; 32.74%); this trend also holds true for other pollutants as well. Southern Hemisphere South America (SHSA) and Northern Hemisphere Africa (NHAF) ranked second and third, accounting for 20.12% (520.55 Tg) and 15.24% (394.26 Tg), respectively. The contributions of each fire type to the global OBB carbon emissions were then quantified. Savanna grasslands were the largest contributor (1209.12 Tg, 46.74%), followed by woody savanna/shrubs (854.71 Tg, 33.04%), tropical forest (313.32 Tg, 12.11%), temperate forest (92.65 Tg, 3.58%), crop (58.06 Tg, 2.24%), temperate evergreen forest (41.65 Tg, 1.61%), and boreal forest (17.37Tg, 0.67%). According to GFED4.1s, the annual average carbon emissions from wildfires in SHAF, SHSA, and NHAF during 2020–2022 were 1271.63 Tg/year, accounting for approximately 64.55% of the global total OBB carbon emissions. Their research findings are similar to the results of this study, which recorded 1761.84 Tg, equivalent to 68.10% of the total.

Specifically, the contributions of the seven fire types to OBB carbon emissions varied dramatically across continents (van der Werf et al., 2010). In SHAF, the primary sources of OBB were savanna grasslands and woody savanna or shrubs, contributing 465.85 (54.99%) and 324.08 Tg/year (38.26%), respectively, consistent with Nguyen et al. (2023). Unlike SHAF, OBB in SHSA primarily originated from savanna grasslands and tropical forests (Shi et al., 2015), contributing 225.86 (43.38%) and 177.17 Tg/year (34.03%) to the region’s carbon emissions, respectively. This variation could be associated with the ecological and climatic conditions unique to each region (Sahu and Sheel, 2014; Santana et al., 2016). South America hosts the world’s largest rainforests and is known for its rich biodiversity and biomass (Fagua and Ramsey, 2019). However, they are severely threatened human–induced deforestation and forest fires (Chen et al., 2013). Studies indicate that forest fires and human activities, such as deforestation and land–use changes, are the main drivers of increased carbon emissions from OBB in this region (Nepstad et al., 1999; Cochrane and Laurance, 2002). In the NHAF, the predominant source of OBB was savanna grasslands (Roberts et al., 2009), contributing 76.14% to the region’s total biomass–burning carbon emissions, averaging 300.21 Tg/year. This may be related to the arid climate and low forest cover in the region (Ichoku et al., 2016; De Sales et al., 2016). Previous research has shown that climate change and human activities, such as grazing and agricultural expansion, are the major factors in this region (Scholes and Andreae, 2000; Flannigan et al., 2009).

Table 4. Annual carbon emissions from global OBB in different regions during 2020–2022 (Unit: Tg/year).

Different Region	Savanna Grasslands	Woody Savanna/Shrubs	Tropical Forest	Temperate Forest	Boreal Forest	Temperate Evergreen Forest	Crop	Total
BONA	4.43	57.55	0.00	0.36	7.58	2.15	0.63	72.70
TENA	41.20	83.89	0.00	5.71	0.00	30.85	4.07	165.72
CEAM	8.62	17.47	4.57	2.33	0.00	0.02	1.11	34.12
NHSA	19.12	11.08	12.23	0.28	0.00	0.00	0.22	42.93
SHSA	225.86	76.69	177.17	27.49	0.00	0.37	12.98	520.56
EURO	5.21	4.60	0.00	0.71	0.19	0.40	1.92	13.03
MIDE	4.95	1.17	0.00	0.15	0.00	0.33	1.78	8.38
NHAF	300.21	47.03	30.31	3.93	0.00	0.00	12.78	394.26
SHAF	465.86	324.09	41.17	12.70	0.00	0.00	3.22	847.04
BOAS	59.51	95.97	0.00	1.29	9.01	0.07	1.50	167.35
CEAS	10.31	7.71	0.68	1.86	0.59	0.33	6.45	27.93
SEAS	21.46	101.57	42.39	22.26	0.00	0.26	9.36	197.30
EQAS	1.43	7.23	4.45	0.02	0.00	0.00	0.08	13.21
AUST	40.95	18.66	0.35	13.57	0.00	6.86	1.97	82.36

Fire events in savanna grasslands remain a major source for most pollutants generated by global OBB, whereas crops contribute relatively less (Figure 3). However, with respect to BC and NH_3, fire events in woody savanna/shrubs have become the primary contributors (BC, 59.40%; NH3, 39.33%). Furthermore, when considering the different regions, the primary sources of pollutants from OBB vary. For instance, fire events in woody savanna/shrubs were the primary sources in the BONA, SEAS, and EQAS regions, whereas crop–related fire events mainly occurred in the EURO, MIDE, CEAS, and SEAS regions.

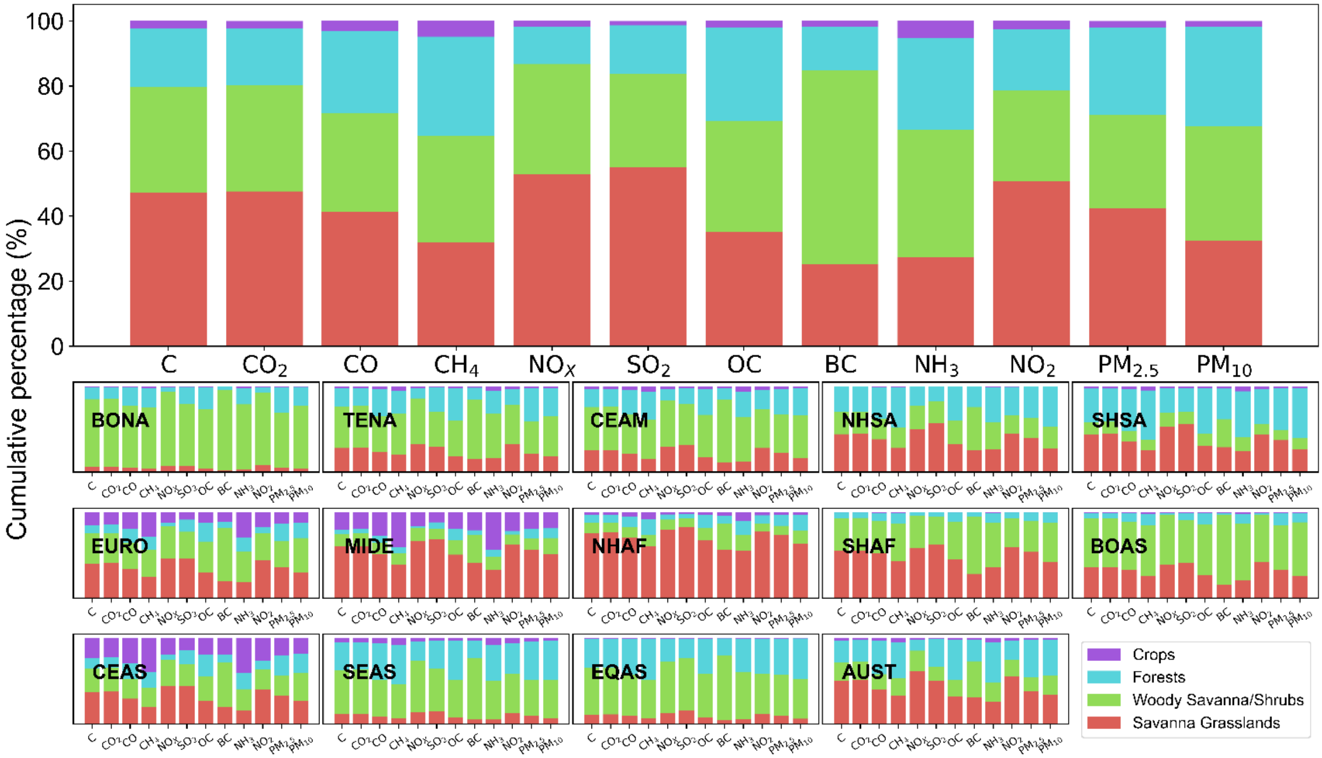

Figure 3: Cumulative percentage of annual OBB emissions for each land type in each region during 2020–2022.

3.2 Temporal variations in OBB carbon emissions

The monthly carbon emissions at both the global and regional levels are illustrated in Figure 4. Overall, global OBB carbon emissions experienced notable shifts, with considerable monthly variations from 2020 to 2022, and peak emissions were observed in Aug 2021 (729.37 Tg). Global OBB carbon emissions were 2,861.05 Tg in 2020, rising slightly to 2,991.15 Tg in 2021, but showing a significant decline to 1,908.41 Tg in 2022. Monthly and seasonal variations in the OBB carbon emissions from each region exhibited substantial differences. Of the 14 regions, the annual contribution of SHAF, the largest global contributor of OBB carbon emissions (32.74%), increased by 2.70% per year, with the peak emission of 283.59 Tg occurring in August 2021. SHAF has emerged as a primary contributor to global OBB carbon emissions owing to its substantial biomass and escalating human activities. Abundant biomass, including dense vegetation and rich forest resources, provides ample fuel for carbon emissions that are exacerbated by intensifying human activities (Chen et al., 2017). In August, specific meteorological conditions, such as high temperatures and low humidity facilitated the increased combustibility of biomass, resulting in a peak in carbon emissions (Shea et al., 1996). Although the SHAF region consistently remained the largest contributor to global OBB carbon emissions during 2020–2022, its annual emissions remained relatively stable, with minor fluctuations. Conversely, emissions from SHSA decreased at a rate of 105.22 Tg per year from 2020 to 2022, with peak monthly emissions over the 3 years reaching 184.63, 222.12, and 123.98, respectively, size and status of emissions consistent with Griffin et al. (2023). Annual C emissions in NHAF also declined, decreasing by 55.44 Tg over the 3 years, with its emissions accounting for the lowest percentage at 13.76% in 2021.

Cumulatively, SHAF, SHSA, and NHAF represent almost 70% of the global OBB carbon emissions, a testament to the profound intertwining of their native ecosystems, land utilization, and climatic influences on biomass combustion (Roy et al., 2022). Deeper exploration revealed that the SHAF, which is endowed with vast stretches of savannahs and grasslands, undergoes intermittent dry periods (Hoffmann and Jackson, 2000). This climatic pattern, combined with entrenched agricultural customs like slash–and–burn, renders the region prone to wildfires (Lourenco et al., 2022). In the SHSA, which covers significant portions of the Amazon rainforest, rampant deforestation often involves controlled burning (Kröger and Nygren, 2020). Unfortunately, these sometimes escalate beyond the control level, adding substantially to emissions figures (Eufemia et al., 2022). In contrast, the NHAF's shifting land–use paradigms, coupled with increasingly recurrent droughts—potentially a byproduct of global warming—intensify frequency of fires in the area (Machete and Dintwe, 2023).

Examination of monthly emissions data revealed significant regional disparities. For example, every January, the NHAF, influenced by its monsoon cycles (Martin and Thorncroft, 2014), consistently emerges as the primary contributor to biomass carbon emissions, accounting for contributions of 50.74%, 81.16%, and 67.66% across the 3 years, as reported by Tsivlidou et al. (2022). By March, SEAS witnessed a surge in emissions, largely due to shifts in forestry practices (Shi et al., 2014), with contributions escalating to 50.82%, 57.78%, and 40.67% in subsequent years (Pletcher et al., 2022), respectively. The peak biomass carbon emissions in 2020 occurred in September, reaching 500.62 Tg. However, the peaks in 2021 and 2022 appeared sooner in August, with emissions of 729.37 Tg and 357.57 Tg, respectively. The 2021 ascent of BONA emissions might be linked to altered land–use guidelines or increased farming activities (Zerriffi et al., 2023) and the many wildfires that occurred (Hoffman et al., 2022), while California's heightened investment in fire mitigation programs (Umunnakwe et al., 2022) and the U.S. Forest Service's implementation of a decade–long strategy (Confronting the Wildfire Crisis, 2023) in 2022 have effectively curbed wildfire incidents in the Temperate North America (TENA) region. This shift in the perception of forest fire management has been instrumental in mitigating wildfire risk in the area. Nevertheless, it is important to acknowledge that the occurrence of wildfires varies over time (Bowman et al., 2017).

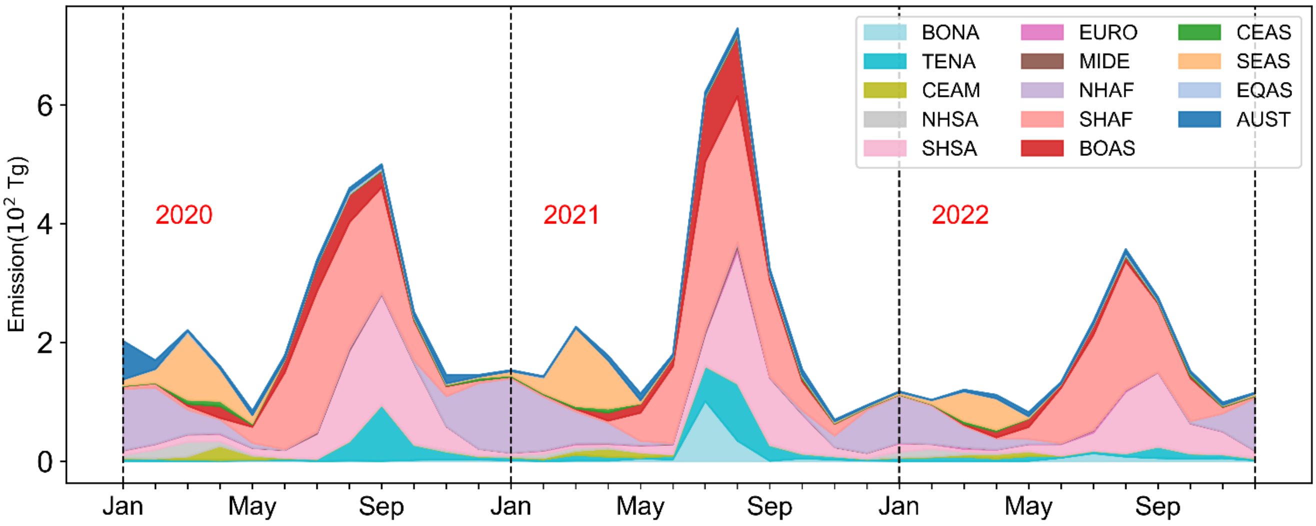

Figure 4: Global OBB carbon emissions in different regions during 2020–2022.

Figure 5 shows the notable temporal fluctuations in global wildfire carbon emissions for different fire types throughout the study period from 2020 to 2022. Global combustion exhibited the highest carbon emissions in August and September. In September 2020, single–month emissions peaked at 500.62 Tg. However, in 2021 and 2022, the zenith of carbon emissions from fires occurred in August, registering at 729.37 and 357.57 Tg respectively. The smaller peaks observed in March should not be overlooked. Interestingly, although the timing of these emission peaks varied, their main contributing factors remained similar. In September, the daily carbon emission peaks from savanna grasslands, woody savanna/shrubs, and tropical forest regions were 7.54 (38%), 7.12 (37%), and 3.36 (31%), respectively. These sources constituted the primary contributors to the global biomass combustion carbon emissions from July to October.

Spatial and temporal variations in global OBB emissions are pronounced because of the differences in ecosystems, climatic conditions, and human activities across different regions (Moritz et al., 2012; Ward et al., 2018). For instance, areas with expansive tropical grasslands, such as Sub–Saharan Africa and Australia, typically experience high levels of OBB emissions because of the prevalence of both natural and anthropogenic fire activities (Williams et al., 2019; Zheng et al., 2021). Moreover, many regions undergo cyclical OBB emission patterns, coinciding with the onset of the dry and wet seasons (Gautam et al., 2013; Dury et al., 2011). The dry season, characterized by an increase in dry biomass and conducive weather conditions, often witnesses a surge in fire activity, resulting in elevated emission levels (Zhang et al., 2023b). These considerable spatial and temporal fluctuations in global OBB emissions mirror the diversity of ecosystems and climatic conditions across various geographic locations (Fagre et al., 2003), which are further influenced by human endeavours and natural fire regimes (Jones et al., 2022).

In 2020 and 2021, significant wildfire events, such as the California wildfires and Australian forest fires, led to an escalation in carbon emissions from fires (Keeley and Syphard, 2021; Safford et al., 2022; Collins et al., 2021; Gallagher et al., 2021; Collins et al., 2022). However, a dual phenomenon was observed in 2022. The implementation of robust wildfire control measures contributed to a reduction in emissions (Wollstein et al., 2022); however, an overall augmentation in annual precipitation led to a reduction in the degree of drought (Thackeray et al., 2022; Zhang et al., 2023a). Consequently, the annual OBB carbon emissions in 2022 were lower than those in the preceding years.

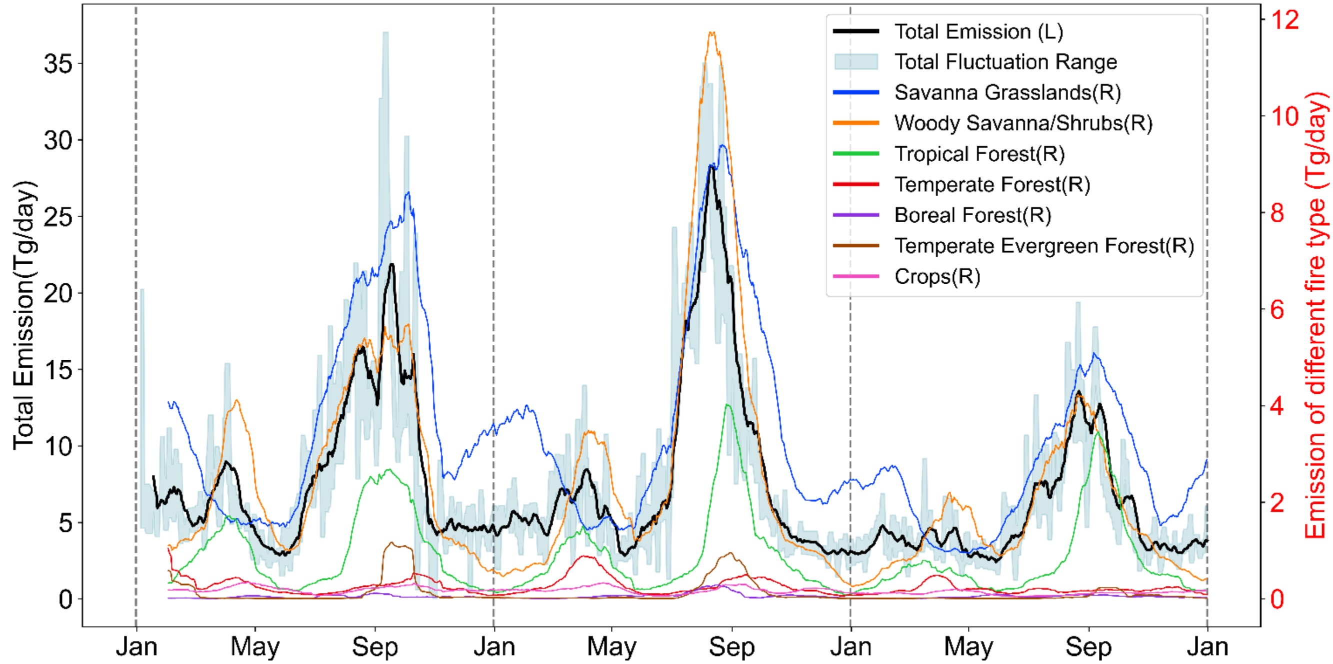

Figure 5: Variations in total global OBB carbon emissions and carbon emissions in different fire types across various regions from 2020 to 2022.

Specifically, carbon emissions resulting from fire events were analysed in 14 global subregions from 2020 to 2022 (Figure 6). This analysis revealed the primary sources of carbon emissions from fires worldwide and provided insights into the main constituents of combustion in different regions. Emission patterns across different global regions vary both temporally and spatially. The top three major emitting regions were SHAF, SHSA, and NHAF, which were closely associated with global emission trends, representing the main source of the emission peak in August and the emission during the winter months. During 2020 to 2022, the OBB conditions in the SHAF, SHSA, and NHAF regions have been relatively stable, with daily peak values of 12.04 Tg, 9.81 Tg and 4.38 Tg respectively. For the SHAF and SHSA, burning activities were predominantly observed from July to September, which can be attributed to a combination of dry weather, strong winds, and specific meteorological conditions (Li et al., 2023; Eames et al., 2023). These factors collectively enhanced the combustibility of the biomass during this period, leading to an increased likelihood of burning. In the SHAF, emissions were primarily influenced by savanna grasslands (49%) and woody savanna/shrubs (47%). Similarly, in the SHSA, emissions were mainly affected by savanna grasslands (34%) and tropical forests (38%). While burning in the NHAF region is concentrated between November and January, primarily in January, this pattern is significantly influenced by the practice of slash–and–burn agriculture (Serrani et al., 2022), with savanna grasslands accounting for 77% of the contributing factors.

CEAM and SEAS exhibited similar wildfire patterns, primarily occurring in March, and a noticeable decrease in burning activity emissions from 2020 to 2022. The predominant fire type in the CEAM region was woody savanna/shrubs (50%), whereas in the SEAS region, it was mainly influenced by woody savanna/shrubs (50%) and tropical forest (25%). Overall, owing to similarities in factors, such as biomass fuel load and climate, the wildfire types in the CEAM and SEAS were quite alike.

The BONA, TENA, EURO, MIDE, BOAS, and AUST share a common characteristic: OBB carbon emissions exhibit a high degree of randomness, indicating their primary influence on natural wildfire events. For instance, British Columbia, Canada, experienced a series of wildfires in July 2021 (Copes-Gerbitz et al., 2022), leading to peak carbon emissions for BONA in 2021 (4.46 Tg). TENA, affected by a series of wildfires in the western United States in 2020 (Safford et al., 2022) and the ongoing wildfires in California in 2021 (Varga et al., 2022), showed elevated emissions in both years (2020, 6.12 Tg; 2021, 3.76 Tg), with woody savanna/shrubs being the main fire event type. For the EURO, the apex of wildfires in 2021 was distinctly shaped by wildfires in Southern and Southeastern Europe (Tedim et al., 2022). The emissions were predominantly associated with fire type savanna grassland (48%). Moreover, in the BOAS region, wildfires were influenced by forest fires in Siberia (Ponomarev et al., 2022), where the principal fire type was woody savanna/shrubs (31%). Regarding AUST, in January 2020, a significant forest fire event occurred (Storey et al., 2023), resulting in peak emission of 4.48 Tg. The primary fire types were temperate forest (24%) and savanna grassland (18%).

The situation of OBB in CEAS is intricate. In March, substantial OBB emissions resulted from agricultural practices, such as slash and burn cultivation and the burning of crop residues (Liu and Shi, 2023), with crops being the predominant fire event type (30%). In contrast, from August to November, OBB was mainly attributed to scorching weather and monsoon conditions (Shi et al., 2018), with savanna grasslands being the dominant type (28%). Recently, owing to improvements in agricultural management practices, there has been a noticeable decrease in OBB events of crop types.

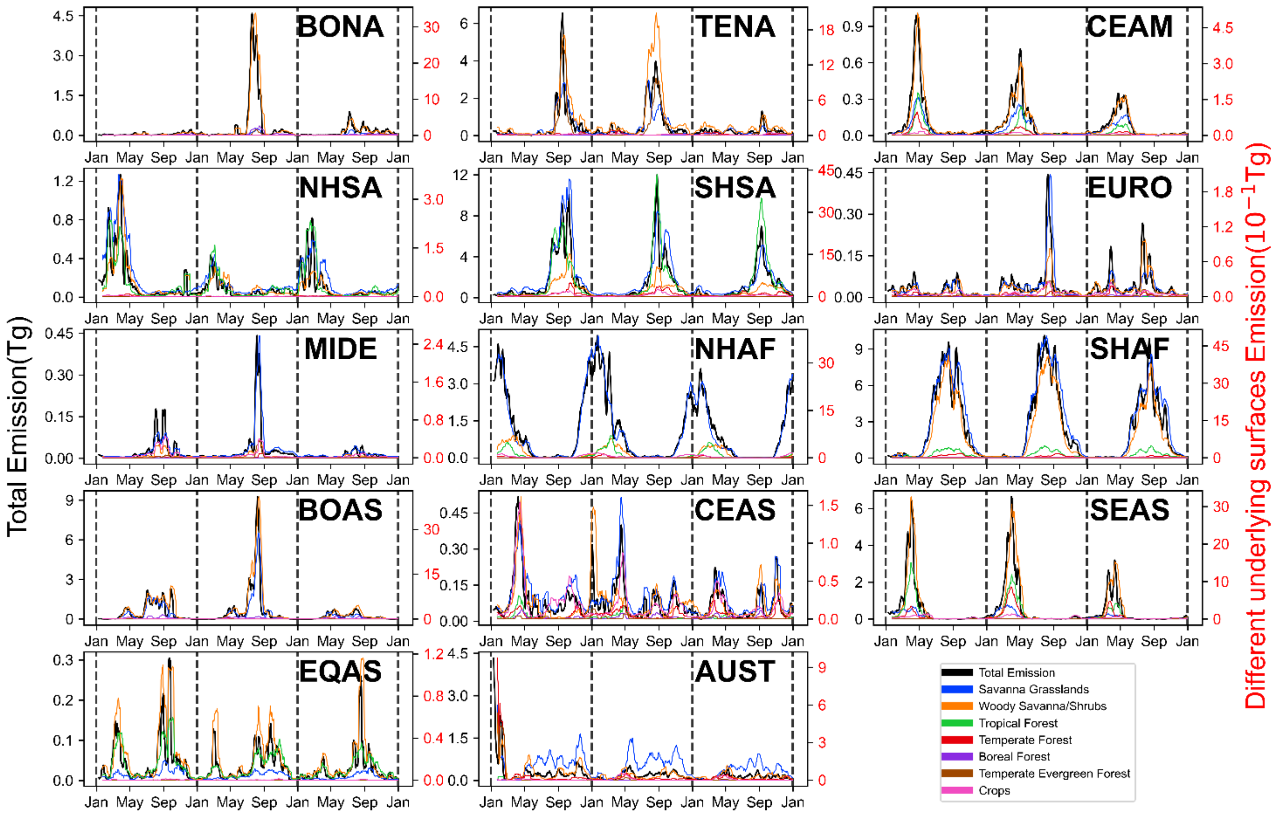

Figure 6: Global OBB emissions for different fire types in different regions (averaged over a 15–day window) from 2020 to 2022.

3.3 Cross–verification in different database

In this study, we juxtaposed the global distribution of OBB carbon emissions as estimated in GEIOBB with data published in the GFAS, GFED, and FEER datasets for 2020–2022 (Figure 7). Overall, our assessments corresponded well with the GFAS, GFED, and FEER, Although there was an overestimation in high–latitude regions, the overall differences across large regions were minimal. For instance, we estimated the total carbon emissions in the BONA region to be 72.71 Tg, while the values from GFAS, GFED, and FEER were 61.21, 125.05, and 35.83 Tg, respectively. This variance can be attributed to the different resolutions (1 km×1 km, 0.1°×0.1°, 0.25°×0.25°, and 0.1°×0.1°) and different estimation methodologies employed. Both our study and the GFED adopted an estimation approach based on the burned area, whereas the GFAS and FEER formulated their inventories based on fire radiative energy. Consequently, our inventory yielded accurate assessment results and captured the spatial variation and heterogeneity of minor OBB emissions effectively, which could have been overlooked in coarse–scale analyses. Additionally, the GFED utilizes MODIS satellite data to calculate the available biomass fuel, whereas we leverage the higher precision and small fire quantification capability of FY–3D GFR data. Disparities between different satellite data and variations in parameter definitions during inventory formulation contribute to these differences. Moreover, we adopted published local measurement–based emission factors and improved correlation coefficients for estimating OBB carbon emissions, which are more reliable and significantly enhance the local emission estimation accuracy.

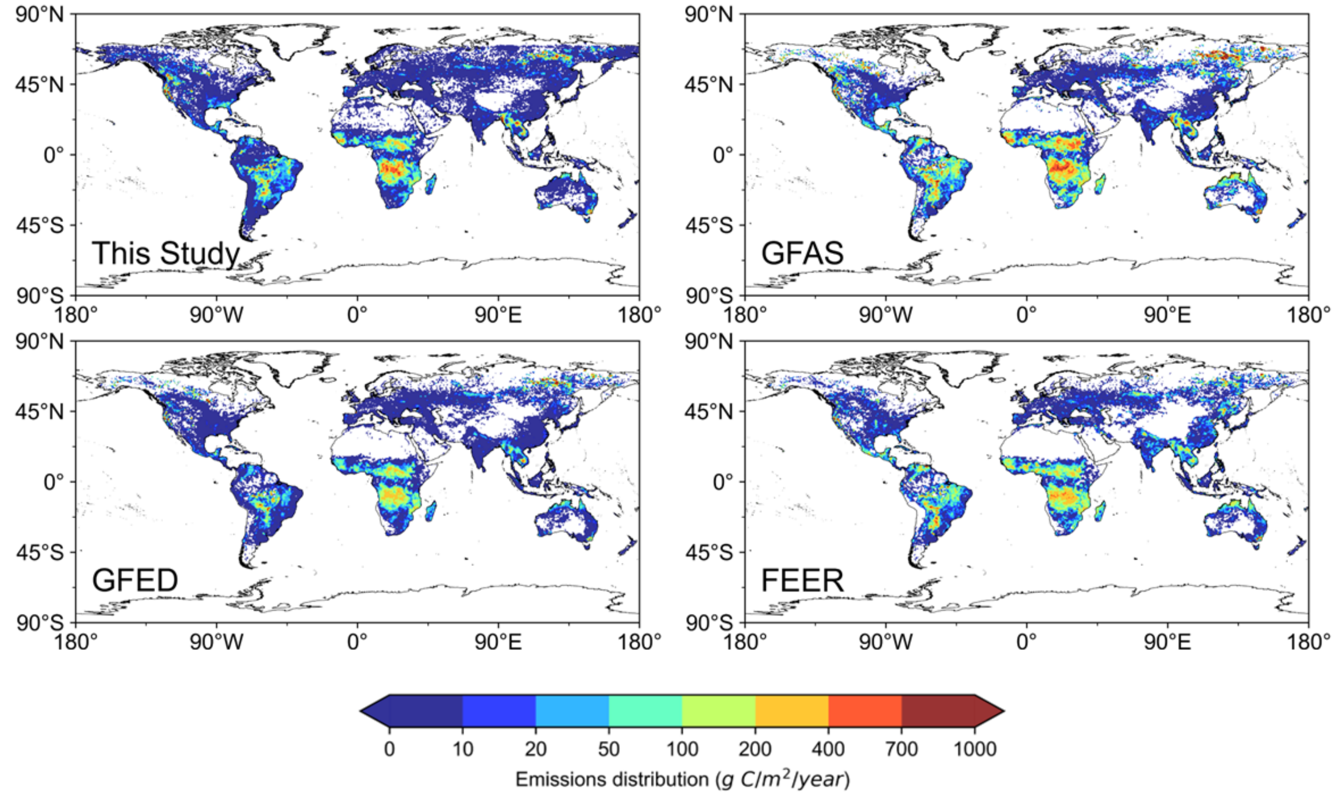

Figure 7: Comparison between this study and other emission inventories during 2020–2022 average emissions at 0.5° resolution.

Specifically, in high emission regions, such as NHAF, NHSA, and CEAS, our estimation of OBB carbon emissions (multi–year average 394.25, 42.93, and 27.93 Tg; monthly peak average 102.52, 11.86, and 6.24 Tg) aligned closely with those of GFED (multi–year average 342.31, 29.10, and 38.16 Tg; monthly peak average 97.58, 9.86, and 10.91 Tg) and GFAS (multi–year average 288.81, 35.80, and 43.51 Tg; monthly peak average 70.65, 9.64, and 9.82 Tg), as illustrated in Figure 8. However, discrepancies were observed between MIDE and EQAS, with FINN notably overestimating carbon emissions from fires. This overestimation by FINN is attributed to its methodology (Wiedinmyer et al., 2011), which relies on a combination of emission factors, conversion rates, and fire radiative energy values to estimate the emissions from agricultural residue burning. This contrasts with our approach, which bases estimates on the burned area and thus can accurately quantify carbon emissions from large fires and reduce uncertainty in fire data (Shi et al., 2020). Additionally, emission estimates during the periods by FINN, GFED, and GFAS were generated using data from the Terra and Aqua satellites, which captured data at 10:30 and 13:30 LT, respectively. Consequently, the burned area algorithm of the GFED cannot effectively detect small, short–lived agricultural fires, which owing to their intermittent nature, occur briefly between the intervals of satellite passes (Giglio et al., 2010). However, the use of FY–3D, which captures data at 14:00, was highly effective in capturing such events.

The AGB values used in this study were directly derived from a dataset generated by combining field and satellite observations (Avitabile et al., 2016). GFED, calculates this value through simulations using the biogeochemical CASA model. While GFED has adjusted turnover rates for herbaceous leaves and surface litter at the ecosystem level to match the observed AGB used in this study, the significant differences in the estimated AGB between biogeochemical model simulations and field measurements are noteworthy (van der Werf et al., 2017). Furthermore, a high–resolution emissions inventory of 1 × 1 km was developed. This inventory allows for the capture and description of spatial variations and heterogeneity in small–scale OBB emissions, providing detailed information on spatial discrepancies that may be missed by large and coarse grid pixels (Shi et al., 2019).

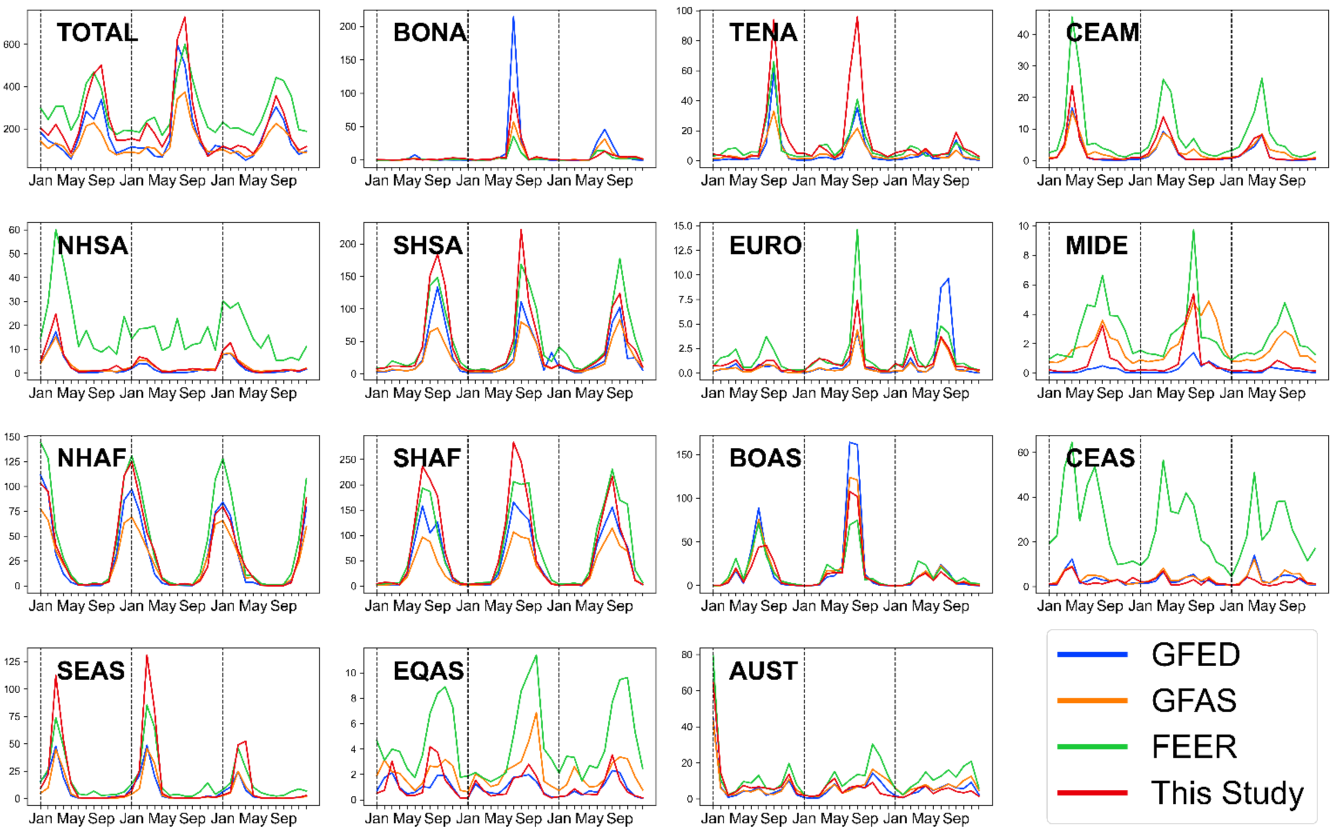

Figure 8: Comparison of monthly emissions in different regions of this and other emission inventories.

We compared and validated the accuracy of monthly OBB carbon emission estimates in 14 global subregions using three global OBB fire products: GFAS, GFED, and FEER. The Taylor diagram illustrates a high degree of consistency between these estimates and other inventories in terms of the standard deviation, correlation coefficient, and amplitude ratio (Figure 9). Overall, the results of this study were closer to the GFED and GFAS inventories, with the best agreement observed with the GFAS inventory. Our results show a correlation coefficient >0.70 ($p < 0.01$) in over 80% of the regions with the other three inventories, indicating a strong positive correlation and consistency in data trends between our study and the other three lists in most regions. Furthermore, in the top three emission source regions, SHAF, SHSA, and NHAF, our correlation coefficients with the other three emission inventories were all >0.90, standard deviation ratios were <2.00, and normalized centered root mean square errors were <0.50. For example, compared with the other three inventories in the NHAF region, the correlation coefficients were all 0.97, with standard deviations of 0.93 (GFED), 0.66 (GFAS), and 1.24 (FEER). However, when compared with the FEER inventory, there were still disparities in the estimated results between the FEER inventory and this study. For instance, in low–emission regions, such as EQAS, NHSA, CEAM, and MIDE, the correlation coefficients ranged from 0.60 to 0.95, with standard deviation exceeding 1.00. This was attributed to FEER's use of the FRE–based approach and overestimation in quantifying small fire points (Ye et al., 2023).

In summary, we demonstrated that the GEIOBB was a dataset with relatively high–quality estimates of global OBB emissions and performed well across all time periods and regions. Overall, a comparison with multiple inventories indicated that our GEIOBB model could effectively capture the spatial and temporal distribution characteristics of OBB at large scales.

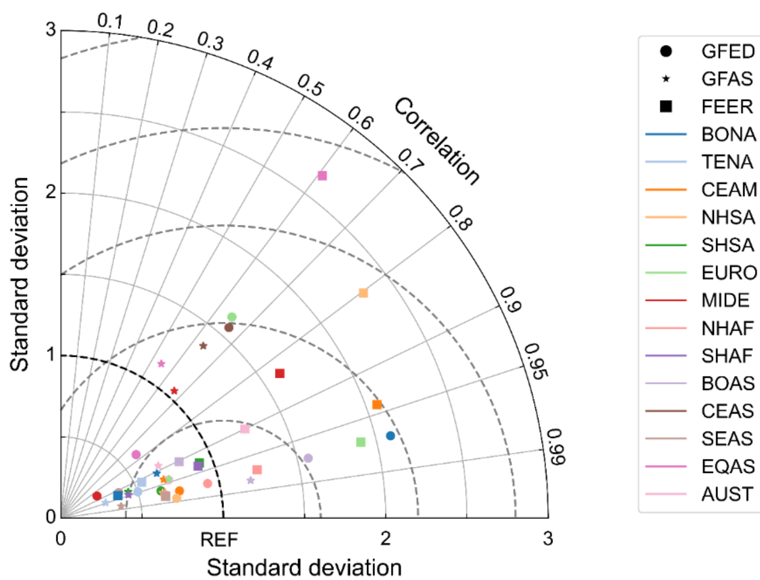

Figure 9: Normalized Taylor diagram plot of the comparison between GFED, GFAS, and FEER and this study with monthly OBB carbon emission.

3.4 Advantages

To create a more accurate and effective biomass combustion carbon emission inventory, our research introduced three significant improvements compared to other inventory products. (1) The input global fire spot monitoring data from FY–3D showed a higher accuracy than MODIS in monitoring active fires (Xian et al., 2021). The OBB emissions exhibited significant consistency with the satellite fire detection results. Existing OBB emission estimation inventories differ mainly in the optimization of relevant parameters and estimation methods; however, they all rely on MODIS fire detection results as their primary data source. Our experiment utilized data from FY–3D GFR, which provides higher precision and the capability to quantify small–scale fire points more accurately (Zhenzhen Yin, 2020) . Consequently, the accuracy of the OBB carbon emissions assessment significantly improved. (2) Satellite and observational AGB resulted in less uncertainty than land cover based available biomass. Previous studies have used fixed values for AGB with regional and land cover–based partitioning. Our research employed AGB inventory data, which, in contrast to the traditional method of regional sub–surface value assignment, better represents spatial variation trends. Additionally, by incorporating dynamic adjustment methods, we mitigated the temporal distribution shortcomings inherent in AGB data. This approach significantly enhances the portrayal of global biomass distribution across both time and space dimensions; (3) Spatially and temporally variable CF scaled by several vegetation indices can reflect a more accurate fraction of burned biomass than the allocated constants based on fire types. We optimized the previous single fixed value or simple formula–based definitions of CF by incorporating numerous parameters to better represent vegetation combustion conditions. To address the varying fire conditions, we performed a detailed subdivision based on different fire types. This advancement over conventional methods of fixed–value assignment or unified fixed–value methods without substrate distinction, enables a more effective computation of burn factors for different types of fires, which can significantly enhance the delineation and understanding of burn factors in the biomass combustion process, paving the way for a more accurate carbon emission inventory. Through these notable improvements, our biomass combustion carbon emissions inventory is a robust tool that provides precise and insightful analyses instrumental for advancement in the field of biomass combustion carbon emissions assessment.

3.5 Uncertainties

There were relatively high uncertainties in the estimation of OBB emissions for the seven types; the uncertainties were associated with the burned area, F, CF, and EF. Although the FY–3D GFR dataset is reliable for most OBB events, its resolution of 1 km results in poor detection performance for small fire points (Zheng et al., 2023). The detected active fires were also underestimated due to cloud cover/thick smoke, with an omission error of approximately from 10%–30% (Schroeder et al., 2008; Roberts et al., 2009; Giglio et al., 2006). Additionally, the uncertainties in the AGB calculations developed by Spawn and Gibbs (2020) ranged from 20% to 80%. Specifically, for approximately 80% of the area, the AGB uncertainties were <30%, whereas in regions, such as Africa and South America, high uncertainties of 60%–70% were observed. The estimated CF shows uncertainties of approximately 20–30% based on empirical formulas (Zhang et al., 2008). The typical uncertainties for trace gas and aerosol emission factors for each land type, as compiled by Shi et al. (2015), ranged from 20% to 50%. Owing to the inherent uncertainties in all input parameters, after estimating the OBB emission inventories, we quantitatively assessed the estimation uncertainties of all emission species using 20,000 Monte Carlo simulations to calculate emission ranges with a 90% confidence interval. Based on this, the emission ranges for different species are as follows: 1,168.02–4,120.83 Tg C, 2.31–5.48 Tg BC, 7.73–25.26 Tg CH_4, 193.11–505.66 Tg CO, 2,994.71–14,153.75 Tg CO_2, 3.31–8.49 Tg of NH_3, 7.92–26.08 Tg NO_2, 12.70–26.87 Tg NO_X, 8.37–29.35 Tg OC, 37.66–84.17 Tg PM_{10}, 19.85–61.62 Tg $PM_{2.5}$, and 1.67–6.69 Tg SO_2.

4 Conclusion

We developed a high–spatial–resolution (1 km×1 km grid) and daily inventory of global OBB emissions. Our inventory used the updated satellite–based burned area product (FY–3D GFR), observational and satellite–based AGB, and vegetation index–based spatiotemporally variable combustion efficiency data to estimate global OBB carbon emissions.

The estimated annual average OBB carbon emissions were 72.71 Tg of BONA, 165.72 Tg of TENA, 34.11 Tg of CEAM, 42.93 Tg of NHSA, 520.54 Tg of SHSA, 13.02 Tg of EURO, 8.37 Tg of MIDE, 394.32 Tg of NHAF, 847.03 Tg of SHAF, 167.35 Tg of BOAS, 27.93 Tg of CEAS, 197.29 Tg of SEAS, 13.20 Tg of EQAS, and 82.37 Tg of AUST. NHAF, as the primary contributor in January, accounted for 50.74%, 81.16%, and 67.66% in the three respective years. During the first peak of the years, March was mainly influenced by increased SEAS emissions (2020: 50.82%, 2021: 57.78%, and 2022: 40.67%). In 2020, the annual peak occurred in September at 500.62 Tg, while in 2021 and 2022, it shifted to August, reaching 729.37 and 357.57 Tg, respectively. Peaks from savanna grasslands, woody savanna/shrubs, and tropical forest regions were 7.54 (38%), 7.12 (37%), and 3.36 Tg (31%), respectively.

We demonstrated that savanna grassland contributed the largest portion (46%) of total emissions, followed by woody savanna/shrubs (33%). Total OBB carbon emissions were the highest from SHAF, followed by SHSA, and NHAF. The fire types where fires occurred were predominantly savanna grasslands, woody savanna/shrubs, and tropical forest in the SHAF, SHSA, and NHAF, and woody savanna/shrubs in SEAS. Furthermore, our data indicate a pronounced seasonal trend in carbon emissions. Regions, such as the SHAF, SHSA, and TENA, played pivotal roles, accounting for the surge in global carbon emissions observed in August.

Our high–spatial–resolution multi–species emission inventory and spatiotemporal characteristics analysis will provide scientific and reliable evidence for formulating carbon emission policies and assessing temporal emission variation. Effective control of the savanna grasslands fire in the SHAF, SHSA, and NHAF as well as tropical forest fires in the SHSA and woody savanna/shrubs fires in the SHAF can greatly reduce carbon emissions. Moreover, this carbon emissions inventory can be used for regional biogeochemical circulation, atmospheric chemical simulations, and environmental health impacts. The accuracy and depth of our findings further underscore the potential for combining our bottom–up approach with top–down satellite observational methods, paving the way for refinement in future studies.

References

Akagi, S. K., Yokelson, R. J., Wiedinmyer, C., Alvarado, M. J., Reid, J. S., Karl, T., Crounse, J. D., and Wennberg, P. O.: Emission factors for open and domestic biomass burning for use in atmospheric models, Atmospheric Chemistry and Physics, 11, 4039–4072, https://doi.org/10.5194/acp-11-4039-2011, 2011.

Anon: A review of biomass burning: Emissions and impacts on air quality, health and climate in China, Science of The Total Environment, 579, 1000–1034, https://doi.org/10.1016/j.scitotenv.2016.11.025, 2017.

Confronting the Wildfire Crisis: https://www.fs.usda.gov/managing-land/wildfire-crisis, last access: 12 October 2023.

Avitabile, V., Herold, M., Heuvelink, G. B. M., Lewis, S. L., Phillips, O. L., Asner, G. P., Armston, J., Ashton, P. S., Banin, L., Bayol, N., Berry, N. J., Boeckx, P., de Jong, B. H. J., DeVries, B., Girardin, C. A. J., Kearsley, E., Lindsell, J. A., Lopez-Gonzalez, G., Lucas, R., Malhi, Y., Morel, A., Mitchard, E. T. A., Nagy, L., Qie, L., Quinones, M. J., Ryan, C. M., Ferry, S. J. W., Sunderland, T., Laurin, G. V., Gatti, R. C., Valentini, R., Verbeeck, H., Wijaya, A., and Willcock, S.: An integrated pan-tropical biomass map using multiple reference datasets, Global Change Biology, 22, 1406–1420, https://doi.org/10.1111/gcb.13139, 2016.

Bowman, D. M. J. S., Williamson, G. J., Abatzoglou, J. T., Kolden, C. A., Cochrane, M. A., and Smith, A. M. S.: Human exposure and sensitivity to globally extreme wildfire events, Nat Ecol Evol, 1, 1–6, https://doi.org/10.1038/s41559-016-0058, 2017.

Bray, C. D., Battye, W., Aneja, V. P., Tong, D. Q., Lee, P., and Tang, Y.: Ammonia emissions from biomass burning in the continental United States, Atmospheric Environment, 187, 50–61, https://doi.org/10.1016/j.atmosenv.2018.05.052, 2018.

Cao, G., Zhang, X., Wang, Y., and Zheng, F.: Estimation of emissions from field burning of crop straw in China, Chin. Sci. Bull., 53, 784–790, https://doi.org/10.1007/s11434-008-0145-4, 2008.

Chen, J., Yao, Q., Chen, Z., Li, M., Hao, Z., Liu, C., Zheng, W., Xu, M., Chen, X., Yang, J., Lv, Q., and Gao, B.: The Fengyun-3D (FY-3D) global active fire product: principle, methodology and validation, Earth System Science Data, 14, 3489–3508, https://doi.org/10.5194/essd-14-3489-2022, 2022.

Chen, Y., Morton, D. C., Jin, Y., Collatz, G. J., Kasibhatla, P. S., van der Werf, G. R., DeFries, R. S., and Randerson, J. T.: Long-term trends and interannual variability of forest, savanna and agricultural fires in South America, Carbon Management, 4, 617–638, https://doi.org/10.4155/cmt.13.61, 2013.

Chen, Y., Morton, D. C., Andela, N., van der Werf, G. R., Giglio, L., and Randerson, J. T.: A pan-tropical cascade of fire driven by El Niño/Southern Oscillation, Nature Clim Change, 7, 906–911, https://doi.org/10.1038/s41558-017-0014-8, 2017.

Cochrane, M. A. and Laurance, W. F.: Fire as a large-scale edge effect in Amazonian forests, Journal of Tropical Ecology, 18, 311–325, https://doi.org/10.1017/S0266467402002237, 2002.

Collins, L., Bradstock, R. A., Clarke, H., Clarke, M. F., Nolan, R. H., and Penman, T. D.: The 2019/2020 mega-fires exposed Australian ecosystems to an unprecedented extent of high-severity fire, Environ. Res. Lett., 16, 044029, https://doi.org/10.1088/1748-9326/abeb9e, 2021.

Collins, L., Clarke, H., Clarke, M. F., McColl Gausden, S. C., Nolan, R. H., Penman, T., and Bradstock, R.: Warmer and drier conditions have increased the potential for large and severe fire seasons across south-eastern Australia, Global Ecology and Biogeography, 31, 1933–1948, https://doi.org/10.1111/geb.13514, 2022.

Copes-Gerbitz, K., Hagerman, S. M., and Daniels, L. D.: Transforming fire governance in British Columbia, Canada: an emerging vision for coexisting with fire, Reg Environ Change, 22, 48, https://doi.org/10.1007/s10113-022-01895-2, 2022.

De Sales, F., Xue, Y., and Okin, G. S.: Impact of burned areas on the northern African seasonal climate from the perspective of regional modeling, Clim Dyn, 47, 3393–3413, https://doi.org/10.1007/s00382-015-2522-4, 2016.

Di Giuseppe, F., Rémy, S., Pappenberger, F., and Wetterhall, F.: Combining fire radiative power observations with the fire weather index improves the estimation of fire emissions, Aerosols/Atmospheric Modelling/Troposphere/Physics (physical properties and processes), https://doi.org/10.5194/acp-2017-790, 2017.

DiMiceli, C., Sohlberg, R., and Townshend, J.: MODIS/Terra Vegetation Continuous Fields Yearly L3 Global 250m SIN Grid V061, https://doi.org/10.5067/MODIS/MOD44B.061, 2022.

Dury, M., Hambuckers, A., Warnant, P., Henrot, A., Favre, E., Ouberdous, M., and François, L.: Responses of European forest ecosystems to 21(st) century climate: assessing changes in interannual variability and fire intensity, iForest: Biogeosciences and Forestry, 4, https://doi.org/10.3832/ifor0572-004, 2011.

Eames, T., Russell-smith, J., Yates, C., Vernooij, R., and Werf, G. van der: Seasonal skew of tropical savanna fires, Copernicus Meetings, https://doi.org/10.5194/egusphere-egu23-13544, 2023.

Eufemia, L., Dias Turetta, A. P., Bonatti, M., Da Ponte, E., and Sieber, S.: Fires in the Amazon Region: Quick Policy Review, Development Policy Review, 40, e12620, https://doi.org/10.1111/dpr.12620, 2022.

Fagre, D. B., Peterson, D. L., and Hessl, A. E.: Taking the Pulse of Mountains: Ecosystem Responses to Climatic Variability, Climatic Change, 59, 263–282, https://doi.org/10.1023/A:1024427803359, 2003.

Fagua J. C. and Ramsey R. D.: Geospatial modeling of land cover change in the Chocó-Darien global ecoregion of South America; One of most biodiverse and rainy areas in the world, PLOS ONE, 14, e0211324, https://doi.org/10.1371/journal.pone.0211324, 2019.

Fang, Z., Deng, W., Zhang, Y., Ding, X., Tang, M., Liu, T., Hu, Q., Zhu, M., Wang, Z., Yang, W., Huang, Z., Song, W., Bi, X., Chen, J., Sun, Y., George, C., and Wang, X.: Open burning of rice, corn and wheat straws: primary emissions, photochemical aging, and secondary organic aerosol formation, Atmospheric Chemistry and Physics, 17, 14821–14839, https://doi.org/10.5194/acp-17-14821-2017, 2017.

Friedl, M. and Sulla-Menashe, D.: MODIS/Terra+Aqua Land Cover Type Yearly L3 Global 500m SIN Grid V061, https://doi.org/10.5067/MODIS/MCD12Q1.061, 2022.

Gallagher, R. V., Allen, S., Mackenzie, B. D. E., Yates, C. J., Gosper, C. R., Keith, D. A., Merow, C., White, M. D., Wenk, E., Maitner, B. S., He, K., Adams, V. M., and Auld, T. D.: High fire frequency and the impact of the 2019–2020 megafires on Australian plant diversity, Diversity and Distributions, 27, 1166–1179, https://doi.org/10.1111/ddi.13265, 2021.

Gautam, R., Hsu, N. C., Eck, T. F., Holben, B. N., Janjai, S., Jantarach, T., Tsay, S.-C., and Lau, W. K.: Characterization of aerosols over the Indochina peninsula from satellite-surface observations during biomass burning pre-monsoon season, Atmospheric Environment, 78, 51–59, https://doi.org/10.1016/j.atmosenv.2012.05.038, 2013.

Giglio, L., Csiszar, I., and Justice, C. O.: Global distribution and seasonality of active fires as observed with the Terra and Aqua Moderate Resolution Imaging Spectroradiometer (MODIS) sensors, Journal of Geophysical Research: Biogeosciences, 111, https://doi.org/10.1029/2005JG000142, 2006.

Giglio, L., Randerson, J. T., van der Werf, G. R., Kasibhatla, P. S., Collatz, G. J., Morton, D. C., and DeFries, R. S.: Assessing variability and long-term trends in burned area by merging multiple satellite fire products, Biogeosciences, 7, 1171–1186, https://doi.org/10.5194/bg-7-1171-2010, 2010.

Griffin, D., Chen, J., Anderson, K., Makar, P., McLinden, C. A., Dammers, E., and Fogal, A.: Towards an improved understanding of wildfire CO emissions: a satellite remote-sensing perspective, EGUsphere, 1–37, https://doi.org/10.5194/egusphere-2023-649, 2023.

Hoffman, K. M., Christianson, A. C., Gray, R. W., and Daniels, L.: Western Canada's new wildfire reality needs a new approach to fire management, Environ. Res. Lett., 17, 061001, https://doi.org/10.1088/1748-9326/ac7345, 2022.

Hoffmann, W. A. and Jackson, R. B.: Vegetation–Climate Feedbacks in the Conversion of Tropical Savanna to Grassland, Journal of Climate, 13, 1593–1602, https://doi.org/10.1175/1520-0442(2000)013<1593:VCFITC>2.0.CO;2, 2000.

Ichoku, C., Ellison, L. T., Willmot, K. E., Matsui, T., Dezfuli, A. K., Gatebe, C. K., Wang, J., Wilcox, E. M., Lee, J., Adegoke, J., Okonkwo, C., Bolten, J., Policelli, F. S., and Habib, S.: Biomass burning, land-cover change, and the hydrological cycle in Northern sub-Saharan Africa, Environ. Res. Lett., 11, 095005, https://doi.org/10.1088/1748-9326/11/9/095005, 2016.

Ito, A. and Penner, J. E.: Global estimates of biomass burning emissions based on satellite imagery for the year 2000, Journal of Geophysical Research: Atmospheres, 109, https://doi.org/10.1029/2003JD004423, 2004.

Jegasothy, E., Hanigan, I. C., Van Buskirk, J., Morgan, G. G., Jalaludin, B., Johnston, F. H., Guo, Y., and Broome, R. A.: Acute health effects of bushfire smoke on mortality in Sydney, Australia, Environment International, 171, 107684, https://doi.org/10.1016/j.envint.2022.107684, 2023.

Jiang, X., Wiedinmyer, C., and Carlton, A. G.: Aerosols from Fires: An Examination of the Effects on Ozone Photochemistry in the Western United States, Environ. Sci. Technol., 46, 11878–11886, https://doi.org/10.1021/es301541k, 2012.

Jones, M. W., Abatzoglou, J. T., Veraverbeke, S., Andela, N., Lasslop, G., Forkel, M., Smith, A. J. P., Burton, C., Betts, R. A., van der Werf, G. R., Sitch, S., Canadell, J. G., Santín, C., Kolden, C., Doerr, S. H., and Le Quéré, C.: Global and Regional Trends and Drivers of Fire Under Climate Change, Reviews of Geophysics, 60, e2020RG000726, https://doi.org/10.1029/2020RG000726, 2022.

Kanabkaew, T. and Kim Oanh, N. T.: Development of Spatial and Temporal Emission Inventory for Crop Residue Field Burning, Environ Model Assess, 16, 453–464, https://doi.org/10.1007/s10666-010-9244-0, 2011.

Keeley, J. E. and Syphard, A. D.: Large California wildfires: 2020 fires in historical context, Fire Ecology, 17, 22, https://doi.org/10.1186/s42408-021-00110-7, 2021.

Kröger, M. and Nygren, A.: Shifting frontier dynamics in Latin America, Journal of Agrarian Change, 20, 364–386, https://doi.org/10.1111/joac.12354, 2020.

van Leeuwen, T. T., van der Werf, G. R., Hoffmann, A. A., Detmers, R. G., Rücker, G., French, N. H. F., Archibald, S., Carvalho Jr., J. A., Cook, G. D., de Groot, W. J., Hély, C., Kasischke, E. S., Kloster, S., McCarty, J. L., Pettinari, M. L., Savadogo, P., Alvarado, E. C., Boschetti, L., Manuri, S., Meyer, C. P., Siegert, F., Trollope, L. A., and Trollope, W. S. W.: Biomass burning fuel consumption rates: a field measurement database, Biogeosciences, 11, 7305–7329, https://doi.org/10.5194/bg-11-7305-2014, 2014.

Li, F., Zhu, Q., Riley, W. J., Zhao, L., Xu, L., Yuan, K., Chen, M., Wu, H., Gui, Z., Gong, J., and Randerson, J. T.: AttentionFire_v1.0: interpretable machine learning fire model for burned-area predictions over tropics, Geoscientific Model Development, 16, 869–884, https://doi.org/10.5194/gmd-16-869-2023, 2023.

Li, W., Li, M., Shi, C., Fang, R., Zhao, Q., Meng, X., Yang, G., and Bai, W.: GPS and BeiDou Differential Code Bias Estimation Using Fengyun-3C Satellite Onboard GNSS Observations, Remote Sensing, 9, 1239, https://doi.org/10.3390/rs9121239, 2017.

Li, X., Wang, S., Duan, L., Hao, J., Li, C., Chen, Y., and Yang, L.: Particulate and Trace Gas Emissions from Open Burning of Wheat Straw and Corn Stover in China, Environ. Sci. Technol., 41, 6052–6058, https://doi.org/10.1021/es0705137, 2007.

Liu, X., Zhang, Y., Huey, L. G., Yokelson, R. J., Wang, Y., Jimenez, J. L., Campuzano-Jost, P., Beyersdorf, A. J., Blake, D. R., Choi, Y., St. Clair, J. M., Crounse, J. D., Day, D. A., Diskin, G. S., Fried, A., Hall, S. R., Hanisco, T. F., King, L. E., Meinardi, S., Mikoviny, T., Palm, B. B., Peischl, J., Perring, A. E., Pollack, I. B., Ryerson, T. B., Sachse, G., Schwarz, J. P., Simpson, I. J., Tanner, D. J., Thornhill, K. L., Ullmann, K., Weber, R. J., Wennberg, P. O., Wisthaler, A., Wolfe, G. M., and Ziemba, L. D.: Agricultural fires in the southeastern U.S. during SEAC4RS: Emissions of trace gases and particles and evolution of ozone, reactive nitrogen, and organic aerosol, Journal of Geophysical Research: Atmospheres, 121, 7383–7414, https://doi.org/10.1002/2016JD025040, 2016.

Liu, X., Huey, L. G., Yokelson, R. J., Selimovic, V., Simpson, I. J., Müller, M., Jimenez, J. L., Campuzano-Jost, P., Beyersdorf, A. J., Blake, D. R., Butterfield, Z., Choi, Y., Crounse, J. D., Day, D. A., Diskin, G. S., Dubey, M. K., Fortner, E., Hanisco, T. F., Hu, W., King, L. E., Kleinman, L., Meinardi, S., Mikoviny, T., Onasch, T. B., Palm, B. B., Peischl, J., Pollack, I. B., Ryerson, T. B., Sachse, G. W., Sedlacek, A. J., Shilling, J. E., Springston, S., St. Clair, J. M., Tanner, D. J., Teng, A. P., Wennberg, P. O., Wisthaler, A., and Wolfe, G. M.: Airborne measurements of western U.S. wildfire emissions: comparison with prescribed burning and air quality implications, Journal of Geophysical Research: Atmospheres, 122, 6108–6129, https://doi.org/10.1002/2016JD026315, 2017.

Liu, Y. and Shi, Y.: Estimates of Global Forest Fire Carbon Emissions Using FY-3 Active Fires Product, Atmosphere, 14, 1575, https://doi.org/10.3390/atmos14101575, 2023.

Liu, Y., Goodrick, S., and Heilman, W.: Wildland fire emissions, carbon, and climate: Wildfire–climate interactions, Forest Ecology and Management, 317, 80–96, https://doi.org/10.1016/j.foreco.2013.02.020, 2014.

Lourenco, M., Woodborne, S., and Fitchett, J. M.: Fire regime of peatlands in the Angolan Highlands, Environ Monit Assess, 195, 78, https://doi.org/10.1007/s10661-022-10704-6, 2022.

Machete, R. L. and Dintwe, K.: Cyclic Trends of Wildfires over Sub-Saharan Africa, Fire, 6, 71, https://doi.org/10.3390/fire6020071, 2023.

Martin, E. R. and Thorncroft, C. D.: The impact of the AMO on the West African monsoon annual cycle, Quarterly Journal of the Royal Meteorological Society, 140, 31–46, https://doi.org/10.1002/qj.2107, 2014.

Mehmood, K., Bao, Y., Saifullah, Bibi, S., Dahlawi, S., Yaseen, M., Abrar, M. M., Srivastava, P., Fahad, S., and Faraj, T. Kh.: Contributions of open biomass burning and crop straw burning to air quality: current research paradigm and future outlooks, Frontiers in Environmental Science, 10, 2022.

Moritz, M. A., Parisien, M.-A., Batllori, E., Krawchuk, M. A., Van Dorn, J., Ganz, D. J., and Hayhoe, K.: Climate change and disruptions to global fire activity, Ecosphere, 3, art49, https://doi.org/10.1890/ES11-00345.1, 2012.

Murdiyarso, D. and Lebel, L.: Local to global perspectives on forest and land fires in Southeast Asia, Mitig Adapt Strat Glob Change, 12, 3–11, https://doi.org/10.1007/s11027-006-9055-4, 2007.

Nepstad, D. C., Verssimo, A., Alencar, A., Nobre, C., Lima, E., Lefebvre, P., Schlesinger, P., Potter, C., Moutinho, P., Mendoza, E., Cochrane, M., and Brooks, V.: Large-scale impoverishment of Amazonian forests by logging and fire, Nature, 398, 505–508, https://doi.org/10.1038/19066, 1999.

Nguyen, H. M., He, J., and Wooster, M. J.: Biomass burning CO, PM and fuel consumption per unit burned area estimates derived across Africa using geostationary SEVIRI fire radiative power and Sentinel-5P CO data, Atmospheric Chemistry and Physics, 23, 2089–2118, https://doi.org/10.5194/acp-23-2089-2023, 2023.

Paton-Walsh, C., Smith, T. E. L., Young, E. L., Griffith, D. W. T., and Guérette, É.-A.: New emission factors for Australian vegetation fires measured using open-path Fourier transform infrared spectroscopy – Part 1: Methods and Australian temperate forest fires, Atmospheric Chemistry and Physics, 14, 11313–11333, https://doi.org/10.5194/acp-14-11313-2014, 2014.

Pfeiffer, M., Spessa, A., and Kaplan, J. O.: A model for global biomass burning in preindustrial time: LPJ-LMfire (v1.0), Geoscientific Model Development, 6, 643–685, https://doi.org/10.5194/gmd-6-643-2013, 2013.

Pivello, V. R.: The Use of Fire in the Cerrado and Amazonian Rainforests of Brazil: Past and Present, fire ecol, 7, 24–39, https://doi.org/10.4996/fireecology.0701024, 2011.

Pletcher, E., Staver, C., and Schwartz, N. B.: The environmental drivers of tree cover and forest–savanna mosaics in Southeast Asia, Ecography, 2022, e06280, https://doi.org/10.1111/ecog.06280, 2022.

Ponomarev, E., Zabrodin, A., and Ponomareva, T.: Classification of Fire Damage to Boreal Forests of Siberia in 2021 Based on the dNBR Index, Fire, 5, 19, https://doi.org/10.3390/fire5010019, 2022.

Qiu, X., Duan, L., Chai, F., Wang, S., Yu, Q., and Wang, S.: Deriving High-Resolution Emission Inventory of Open Biomass Burning in China based on Satellite Observations, Environ. Sci. Technol., 50, 11779–11786, https://doi.org/10.1021/acs.est.6b02705, 2016.

Richardson, D., Black, A. S., Irving, D., Matear, R. J., Monselesan, D. P., Risbey, J. S., Squire, D. T., and Tozer, C. R.: Global increase in wildfire potential from compound fire weather and drought, npj Clim Atmos Sci, 5, 1–12, https://doi.org/10.1038/s41612-022-00248-4, 2022.

Roberts, G., Wooster, M. J., and Lagoudakis, E.: Annual and diurnal african biomass burning temporal dynamics, Biogeosciences, 6, 849–866, https://doi.org/10.5194/bg-6-849-2009, 2009.

Roy, P. S., Ramachandran, R. M., Paul, O., Thakur, P. K., Ravan, S., Behera, M. D., Sarangi, C., and Kanawade, V. P.: Anthropogenic land use and land cover changes—a review on its environmental consequences and climate change, J Indian Soc Remote Sens, 50, 1615–1640, https://doi.org/10.1007/s12524-022-01569-w, 2022.

Safford, H. D., Paulson, A. K., Steel, Z. L., Young, D. J. N., and Wayman, R. B.: The 2020 California fire season: A year like no other, a return to the past or a harbinger of the future?, Global Ecology and Biogeography, 31, 2005–2025, https://doi.org/10.1111/geb.13498, 2022.

Sahu, L. K. and Sheel, V.: Spatio-temporal variation of biomass burning sources over South and Southeast Asia, J Atmos Chem, 71, 1–19, https://doi.org/10.1007/s10874-013-9275-4, 2014.

Santana V. M., Alday J. G., Lee H., Allen K. A., and Marrs R. H.: Modelling Carbon Emissions in Calluna vulgaris–Dominated Ecosystems when Prescribed Burning and Wildfires Interact, PLOS ONE, 11, e0167137, https://doi.org/10.1371/journal.pone.0167137, 2016.

Santiago-De La Rosa, N., González-Cardoso, G., Figueroa-Lara, J. de J., Gutiérrez-Arzaluz, M., Octaviano-Villasana, C., Ramírez-Hernández, I. F., and Mugica-Álvarez, V.: Emission factors of atmospheric and climatic pollutants from crop residues burning, Journal of the Air & Waste Management Association, 68, 849–865, https://doi.org/10.1080/10962247.2018.1459326, 2018.

Schroeder, W., Csiszar, I., and Morisette, J.: Quantifying the impact of cloud obscuration on remote sensing of active fires in the Brazilian Amazon, Remote Sensing of Environment, 112, 456–470, https://doi.org/10.1016/j.rse.2007.05.004, 2008.

Senande-Rivera, M., Insua-Costa, D., and Miguez-Macho, G.: Spatial and temporal expansion of global wildland fire activity in response to climate change, Nat Commun, 13, 1208, https://doi.org/10.1038/s41467-022-28835-2, 2022.

Serrani, D., Cocco, S., Cardelli, V., D’Ottavio, P., Rafael, R. B. A., Feniasse, D., Vilanculos, A., Fernández-Marcos, M. L., Giosué, C., Tittarelli, F., and Corti, G.: Soil fertility in slash and burn agricultural systems in central Mozambique, Journal of Environmental Management, 322, 116031, https://doi.org/10.1016/j.jenvman.2022.116031, 2022.

Shan, T. and Zheng, W.: Extraction method of burned area using GF-1 WFV images and FY-3D MERSI fire point products, zggx, null, 1–11, https://doi.org/10.11834/jrs.20221552, 2022.

Shea, R. W., Shea, B. W., Kauffman, J. B., Ward, D. E., Haskins, C. I., and Scholes, M. C.: Fuel biomass and combustion factors associated with fires in savanna ecosystems of South Africa and Zambia, Journal of Geophysical Research: Atmospheres, 101, 23551–23568, https://doi.org/10.1029/95JD02047, 1996.

Shi, Y., Sasai, T., and Yamaguchi, Y.: Spatio-temporal evaluation of carbon emissions from biomass burning in Southeast Asia during the period 2001–2010, Ecological Modelling, 272, 98–115, https://doi.org/10.1016/j.ecolmodel.2013.09.021, 2014.

Shi, Y., Matsunaga, T., and Yamaguchi, Y.: High-Resolution Mapping of Biomass Burning Emissions in Three Tropical Regions, Environ. Sci. Technol., 49, 10806–10814, https://doi.org/10.1021/acs.est.5b01598, 2015.

Shi, Y., Matsunaga, T., Yamaguchi, Y., Li, Z., Gu, X., and Chen, X.: Long-term trends and spatial patterns of satellite-retrieved PM2.5 concentrations in South and Southeast Asia from 1999 to 2014, Science of The Total Environment, 615, 177–186, https://doi.org/10.1016/j.scitotenv.2017.09.241, 2018.

Shi, Y., Zhao, A., Matsunaga, T., Yamaguchi, Y., Zang, S., Li, Z., Yu, T., and Gu, X.: High-resolution inventory of mercury emissions from biomass burning in tropical continents during 2001–2017, Science of The Total Environment, 653, 638–648, https://doi.org/10.1016/j.scitotenv.2018.10.420, 2019.

Shi, Y., Zang, S., Matsunaga, T., and Yamaguchi, Y.: A multi-year and high-resolution inventory of biomass burning emissions in tropical continents from 2001–2017 based on satellite observations, Journal of Cleaner Production, 270, 122511, https://doi.org/10.1016/j.jclepro.2020.122511, 2020.

Spawn, S. A. and Gibbs, H. K.: Vegetation CollectionGlobal Aboveground and Belowground Biomass Carbon Density Maps for the Year 2010, 9810.740697000001 MB, https://doi.org/10.3334/ORNLDAAC/1763, 2020.

Stockwell, C. E., Veres, P. R., Williams, J., and Yokelson, R. J.: Characterization of biomass burning emissions from cooking fires, peat, crop residue, and other fuels with high-resolution proton-transfer-reaction time-of-flight mass spectrometry, Atmospheric Chemistry and Physics, 15, 845–865, https://doi.org/10.5194/acp-15-845-2015, 2015.

Storey, M. A., Price, O. F., and Fox-Hughes, P.: The influence of regional wind patterns on air quality during forest fires near Sydney, Australia, Science of The Total Environment, 905, 167335, https://doi.org/10.1016/j.scitotenv.2023.167335, 2023.

Tedim, F., Leone, V., Lovreglio, R., Xanthopoulos, G., Chas-Amil, M.-L., Ganteaume, A., Efe, R., Royé, D., Fuerst-Bjeliš, B., Nikolov, N., Musa, S., Milenković, M., Correia, F., Conedera, M., and Boris Pezzatti, G.: Forest Fire Causes and Motivations in the Southern and South-Eastern Europe through Experts' Perception and Applications to Current Policies, Forests, 13, 562, https://doi.org/10.3390/f13040562, 2022.

Thackeray, C. W., Hall, A., Norris, J., and Chen, D.: Constraining the increased frequency of global precipitation extremes under warming, Nat. Clim. Chang., 12, 441–448, https://doi.org/10.1038/s41558-022-01329-1, 2022.

Tsivlidou, M., Sauvage, B., Barret, B., Wolff, P., Clark, H., Bennouna, Y., Blot, R., Boulanger, D., Nédélec, P., Le Flochmoën, E., and Thouret, V.: Tropical tropospheric ozone and carbon monoxide distributions: characteristics, origins and control factors, as seen by IAGOS and IASI, Atmospheric Chemistry and Physics Discussions, 1–50, https://doi.org/10.5194/acp-2022-686, 2022.

Umunnakwe, A., Parvania, M., Nguyen, H., Horel, J. D., and Davis, K. R.: Data-driven spatio-temporal analysis of wildfire risk to power systems operation, IET Generation, Transmission & Distribution, 16, 2531–2546, https://doi.org/10.1049/gtd2.12463, 2022.

Urbanski, S.: Wildland fire emissions, carbon, and climate: Emission factors, Forest Ecology and Management. 317: 51-60., 51–60, https://doi.org/10.1016/j.foreco.2013.05.045, 2014.

Varga, K., Jones, C., Trugman, A., Carvalho, L. M. V., McLoughlin, N., Seto, D., Thompson, C., and Daum, K.: Megafires in a Warming World: What Wildfire Risk Factors Led to California's Largest Recorded Wildfire, Fire, 5, 16, https://doi.org/10.3390/fire5010016, 2022.

Ward, D. S., Shevliakova, E., Malyshev, S., and Rabin, S.: Trends and Variability of Global Fire Emissions Due To Historical Anthropogenic Activities, Global Biogeochemical Cycles, 32, 122–142, https://doi.org/10.1002/2017GB005787, 2018.

van Wees, D., van der Werf, G. R., Randerson, J. T., Rogers, B. M., Chen, Y., Veraverbeke, S., Giglio, L., and Morton, D. C.: Global biomass burning fuel consumption and emissions at 500 m spatial resolution based on the Global Fire Emissions Database (GFED), Geoscientific Model Development, 15, 8411–8437, https://doi.org/10.5194/gmd-15-8411-2022, 2022.

van der Werf, G. R., Randerson, J. T., Giglio, L., Collatz, G. J., Mu, M., Kasibhatla, P. S., Morton, D. C., DeFries, R. S., Jin, Y., and van Leeuwen, T. T.: Global fire emissions and the contribution of deforestation, savanna, forest, agricultural, and peat fires (1997–2009), Atmospheric Chemistry and Physics, 10, 11707–11735, https://doi.org/10.5194/acp-10-11707-2010, 2010.

van der Werf, G. R., Randerson, J. T., Giglio, L., van Leeuwen, T. T., Chen, Y., Rogers, B. M., Mu, M., van Marle, M. J. E., Morton, D. C., Collatz, G. J., Yokelson, R. J., and Kasibhatla, P. S.: Global fire emissions estimates during 1997–2016, Earth System Science Data, 9, 697–720, https://doi.org/10.5194/essd-9-697-2017, 2017.

Wiedinmyer, C., Quayle, B., Geron, C., Belote, A., McKenzie, D., Zhang, X., O'Neill, S., and Wynne, K. K.: Estimating emissions from fires in North America for air quality modeling, Atmospheric Environment, 40, 3419–3432, https://doi.org/10.1016/j.atmosenv.2006.02.010, 2006.

Wiedinmyer, C., Akagi, S. K., Yokelson, R. J., Emmons, L. K., Al-Saadi, J. A., Orlando, J. J., and Soja, A. J.: The Fire INventory from NCAR (FINN): a high resolution global model to estimate the emissions from open burning, Geoscientific Model Development, 4, 625–641, https://doi.org/10.5194/gmd-4-625-2011, 2011.

Williams, A. P., Abatzoglou, J. T., Gershunov, A., Guzman-Morales, J., Bishop, D. A., Balch, J. K., and Lettenmaier, D. P.: Observed Impacts of Anthropogenic Climate Change on Wildfire in California, Earth's Future, 7, 892–910, https://doi.org/10.1029/2019EF001210, 2019.

Wollstein, K., Creutzburg, M. K., Dunn, C., Johnson, D. D., O'Connor, C., and Boyd, C. S.: Toward integrated fire management to promote ecosystem resilience, Rangelands, 44, 227–234, https://doi.org/10.1016/j.rala.2022.01.001, 2022.

Wu, J., Kong, S., Wu, F., Cheng, Y., Zheng, S., Yan, Q., Zheng, H., Yang, G., Zheng, M., Liu, D., Zhao, D., and Qi, S.: Estimating the open biomass burning emissions in central and eastern China from 2003 to 2015 based on satellite observation, Atmospheric Chemistry and Physics, 18, 11623–11646, https://doi.org/10.5194/acp-18-11623-2018, 2018.

Wu, M., Luo, J., Huang, T., Lian, L., Chen, T., Song, S., Wang, Z., Ma, S., Xie, C., Zhao, Y., Mao, X., Gao, H., and Ma, J.: Effects of African BaP emission from wildfire biomass burning on regional and global environment and human health, Environment International, 162, 107162, https://doi.org/10.1016/j.envint.2022.107162, 2022.

Xian, D., Zhang, P., Gao, L., Sun, R., Zhang, H., and Jia, X.: Fengyun meteorological satellite products for earth system science applications, Adv. Atmos. Sci., 38, 1267–1284, https://doi.org/10.1007/s00376-021-0425-3, 2021.

Xingcheng Y. a. O., Tiantian Q. U., Wenjing C., Jun Y. I. N., Yongjin L. I., Zhenzhong S. U. N., and Hui Z.: Estimation of grassland biomass using MODIS data and plant community characteristics, zgstnyxb, 25, 530–541, https://doi.org/10.13930/j.cnki.cjea.160931, 2017.

Ye, X., Cheng, T., Li, X., and Zhu, H.: Impact of satellite AOD data on top-down estimation of biomass burning particulate matter emission, Science of The Total Environment, 864, 161055, https://doi.org/10.1016/j.scitotenv.2022.161055, 2023.

You, C. and Xu, C.: Delayed wildfires in 2020 promote snowpack melting in the western United States, Proceedings of the National Academy of Sciences, 120, e2218087120, https://doi.org/10.1073/pnas.2218087120, 2023.

Zerriffi, H., Reyes, R., and Maloney, A.: Pathways to sustainable land use and food systems in Canada, Sustain Sci, 18, 389–406, https://doi.org/10.1007/s11625-022-01213-z, 2023.

Zhang, X., Kondragunta, S., Schmidt, C., and Kogan, F.: Near real time monitoring of biomass burning particulate emissions (PM2.5) across contiguous United States using multiple satellite instruments, Atmospheric Environment, 42, 6959–6972, https://doi.org/10.1016/j.atmosenv.2008.04.060, 2008.

Zhang, X., Duan, J., Cherubini, F., and Ma, Z.: A global daily evapotranspiration deficit index dataset for quantifying drought severity from 1979 to 2022, Sci Data, 10, 824, https://doi.org/10.1038/s41597-023-02756-1, 2023a.

Zhang, Z., Zhang, L., Xu, H., Creed, I. F., Blanco, J. A., Wei, X., Sun, G., Asbjornsen, H., and Bishop, K.: Forest water-use efficiency: Effects of climate change and management on the coupling of carbon and water processes, Forest Ecology and Management, 534, 120853, https://doi.org/10.1016/j.foreco.2023.120853, 2023b.

Zheng, B., Ciais, P., Chevallier, F., Chuvieco, E., Chen, Y., and Yang, H.: Increasing forest fire emissions despite the decline in global burned area, Science Advances, 7, eabh2646, https://doi.org/10.1126/sciadv.abh2646, 2021.

Zheng, W. and Chen, J.: Fire monitoring based on FY-3D/MERSI-II far-infrared data, 红外与毫米波学报, 39, 120–127, https://doi.org/10.11972/j.issn.1001-9014.2020.01.016, 2020.

Zheng, W., Chen, J., Yan, H., Liu, C., Tang, S., and 国家卫星气象中心， 北京 100081 National Satellite Meteorological Center， Beijing 100081， China: Global fire monitoring products of FY-3D/MERSI-II and their applications, National Remote Sensing Bulletin, 24, 521–530, https://doi.org/10.11834/jrs.20209177, 2020.

Zheng, W., Chen, J., Liu, C., Shan, T., and Yan, H.: Study of the Application of FY-3D/MERSI-II Far-Infrared Data in Wildfire Monitoring, Remote Sensing, 15, 4228, https://doi.org/10.3390/rs15174228, 2023.

Zhenzhen Yin, F. C.: Active Fire Monitoring based on FY-3D MERSI Satellite Data, Remote Sensing Technology and Application, 35, 1099–1108, https://doi.org/10.11873/j.issn.1004-0323.2020.5.1099, 2020.